

THE TECTONOMETAMORPHIC EVOLUTION OF THE GREATER HIMALAYAN  
SEQUENCE ALONG THE ZANSKAR SHEAR ZONE, NW INDIA

AS

35

2015

GEOL

•B37

A thesis submitted to the faculty of  
San Francisco State University  
In partial fulfillment of  
the requirements for  
the Degree

Master of Science

In

Geosciences

by

Seniha Ozum Basta

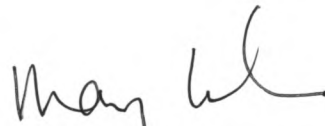
San Francisco, California

January 2015

Copyright by  
Seniha Ozum Basta  
2015

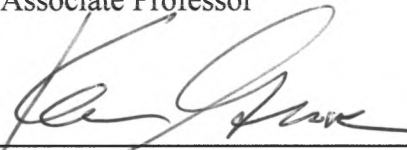
CERTIFICATION OF APPROVAL

I certify that I have read The Tectonometamorphic Evolution of the Greater Himalayan Sequence along the Zaskar Shear Zone, NW India by Seniha Ozum Basta, and that in my opinion this work meets the criteria for approving a thesis submitted in partial fulfillment of the requirement for the degree Master of Science in Geoscience at San Francisco State University.



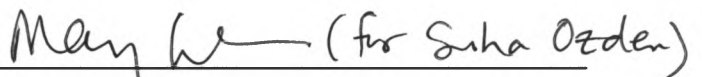
---

Mary Leech, Ph.D.  
Associate Professor



---

Karen Grove, Ph.D.  
Professor



---

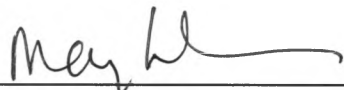
Suha Ozden, Ph.D.  
Professor

The Tectonometamorphic Evolution of the Greater Himalayan Sequence Along the  
Zaskar Shear Zone, NW India

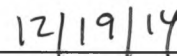
Seniha Ozum Basta  
San Francisco, California  
2015

The Greater Himalayan Sequence (GHS) includes high-grade rocks and granites that have been exhumed along the Zaskar Shear Zone (ZSZ) in the Zaskar region of the western Himalaya. GHS rocks in the Suru Valley record metamorphism and deformation during the Himalayan collision and Miocene exhumation. The prograde regional metamorphic event ( $M_1$ ) is associated with burial of GHS rocks during the Himalayan orogeny, and a retrograde metamorphic event ( $M_2$ ) that is associated with reactivation of the ZSZ as a detachment and exhumation of high-grade rocks. Mineral assemblages consist of  $Qz + Pl + Bt + Ms \pm Grt \pm St \pm Ky \pm Sil \pm And \pm Chl \pm Crd \pm Zo \pm Tur \pm Rt \pm Zrn \pm Opq$ . Field and petrographic observations indicate metamorphic grade in the GHS increases from the chlorite-biotite to the kyanite zone from E to W along the Suru River, and comprising a complete succession of prograde Barrovian-type metamorphism. Rotated garnets, recrystallized quartz grains, irregular grain boundaries, kink bands, microfolds, deformation bands, changes in grain size, and variable crenulation cleavage development suggest different deformation mechanisms and temperatures corresponding to decreasing strain with distance from the ZSZ. Shear sense indicators show that a top-to-the-SW thrusting was overprinted by a top-to-the-NE normal-sense shearing along the ZSZ. Strain is greatest within the ZSZ and seen as reduced grain size, interlobate grain boundaries, anhedral quartz grains, and inequigranular size distribution. Metamorphic temperatures are highest in the structurally-deepest rocks near the Suru Dome in which quartz grains show dynamic recrystallization and late fibrolitic sillimanite growth. Modeled peak P-T conditions for schists from the study area indicate  $\sim 1.18-1.23$  GPa at  $\sim 550-590$  °C for  $M_1$  metapelites from the garnet zone, and  $\sim 1.10$  GPa at  $\sim 625$  °C for  $M_2$  rocks from the kyanite zone in the Suru Dome. While temperature increases from the ZSZ toward the Suru Dome, the Suru Dome records lower pressures related to the late  $M_2$  doming event. U-Pb zircon analyses give ages of  $21.6 \pm 2.7$  to  $17.2 \pm 5.3$  Ma for the period at the end of the  $M_1$  event and the beginning of the  $M_2$  retrogression, and that coincide with the reactivation of the ZSZ as an extensional structure. The late-stage doming event in the early part of the  $M_2$  occurred at  $19.9 \pm 0.9$  Ma.

I certify that the abstract is a correct representation of the content of this thesis.



Chair, Thesis Committee



Date

## ACKNOWLEDGEMENTS

Firstly, I would like to thank Dr. Mary Leech for the opportunity to work on the project. Her insight and guidance gave me inspiration to keep working under hard conditions such as studying in another language and being homesick. Her corrections of my writing were greatly appreciated. I would also like to thank my committee members, Dr. Karen Grove and Dr. Suha Ozden, for their feedback and support. I am also indebted to Theodore Burlick for saving my life a couple of times while working in the Himalayas and his great contributions to this study. I thank Bob Jones at Stanford University for his great help with microprobe analysis and Matt Coble for U-Pb geochronology, and Emma Beck for collaboration with the field work. A special thanks to Dr. Huseyin Yalcin and Dr. Taner Ekici for their mineralogical contributions, and to Halil Karakas for his technical support.

Financial support for this project was received through a NSF CAREER grant (EAR-0847721 to M.L. Leech) jointly supported by the Tectonics, Petrology & Geochemistry, and Education & Human Resources programs. I also would like to thank Turkish Petroleum Corporation for deeming me suitable for a scholarship to support me during my entire master's education. Also many thanks to the Pestrong Grant to support this study.

Finally, I would like to thank my family for giving me life energy with their existence which was all I needed to be able to handle difficulties abroad. I dedicate this study to my father Ozkan Basta who is the most inspirational geologist I have ever known.

## TABLE OF CONTENTS

List of Figures .....	viii
List of Tables .....	ix
1. Introduction.....	1
2. Geologic Setting.....	2
2.1. Regional Geology of the Zaskar Himalaya.....	2
2.2. The Study Area: The Suru Valley in the Zaskar Region .....	4
3. Methods .....	5
3.1. Macrostructural Observations.....	5
3.2. Petrography and Microstructural Analysis .....	6
3.3. Thermobarometry and Metamorphic Modeling.....	7
3.3.1. Construction of Pressure-Temperature Path Segments.....	8
3.4. Geochronology.....	9
4. Results.....	13
4.1. Microstructural Evolution.....	13
4.2. Metamorphic History .....	16
4.2.1. Prograde Metamorphism and Metamorphic Isograds.....	16
The Chlorite-Biotite Zone.....	18
The Garnet Zone .....	19
The Staurolite Zone.....	20
The Kyanite Zone .....	21
4.2.2. Retrograde Metamorphism .....	21

4.3. Quatitative Pressure-Temperature Paths .....	23
4.3.1. Mineral Chemistries .....	23
4.3.2. Pressure-Temperature Constraints .....	24
4.4. U-Pb Zircon Geochronology.....	25
5. Discussion .....	27
5.1. Metamorphic Implications of the Zanskar Region .....	27
5.2. Timing of Metamorphism in the Zanskar Himalaya.....	28
5.3. Tectonometamorphic Evolution of the Zanskar Himalaya .....	30
6. Conclusions.....	35
References .....	38

## LIST OF FIGURES

Figure	Page
1. Regional map .....	48
2. Suru Valley isograd map.....	49
3. Field and outcrop photographs.....	50
4. Photomicrographs for shear sense indicators.....	51
5. Photomicrographs for shear sense indicators.....	52
6. Photomicrographs of representative rock fabrics.....	53
7. Photomicrographs of quartz deformation .....	54
8. Topographic profile and associated photomicrographs of textural changes .....	55
9. Isochemical phase diagrams of sample ZH-31 .....	56-57
10. Isochemical phase diagrams of sample sample ZH-34.....	58-59
11. Isochemical phase diagrams of sample ZH-39 .....	60-61
12. Isochemical phase diagrams of sample ZH-43 .....	62-63
13. Cumulative P-T paths of select samples .....	64
14. Integrated P-T path with geochronologic constraints .....	65
15. U-Pb concordia diagrams .....	66

## LIST OF TABLES

Table	Page
1. Mineral assemblages of representative samples .....	67
2. Mineral abbreviations .....	68
3. XRF geochemical data .....	69
4. WDS-EMPA representative mineral compositions .....	70-72
5. U-Pb SHRIMP zircon data.....	73
6. Chronologic summary of tectonometamorphic events .....	74

## 1. INTRODUCTION

The nearly 2,500 km-long Himalayas are an ideal study area to improve our understanding of mountain-building processes created by continent-continent collision which are among the most prominent geologic features on Earth's surface. The collision between India and Asia likely started during the Paleocene to Early Eocene based on several different lines of evidence (e.g., Searle et al, 1987; Gaetani and Garzanti, 1991; Klootwijk et al., 1992; Garzanti et al., 1996; Rowley, 1996; Searle et al, 1997; De Celles et al., 2002; 2004; Guillot et al., 2003; Leech et al., 2005), and created the largest active continental collision zone in the world. The Himalaya preserve large-scale extensional structures (e.g., the South Tibetan Detachment System, or STDS) that exhumes high-grade rocks which allows the study of mid- to lower crustal processes within this compressional system (i.e., Noble and Searle, 1995; Vance and Harris, 1999; Godin et al., 2001; Walker et al., 2001).

The Himalayas are divided into three primary tectonostratigraphic units that occur in roughly parallel belts: the Tethyan Himalayan Sequence (THS), the Greater (or High) Himalaya Sequence (GHS), and the Lesser Himalayan Sequence (LHS). The primary focus of this research is the GHS which contains high-grade metamorphic rocks and is separated from lower-grade rocks of the LHS by the Main Central Thrust (MCT) to the south, and from the weakly- to unmetamorphosed rocks of the THS by the STDS to the north (Fig. 1a). These north-dipping fault systems were active simultaneously since at least the Miocene (24-12 Ma; Frank et al., 1977, Burchfiel et al., 1992; Vannay and Hodges, 1996; Coleman, 1998; Harris et al., 2004; Godin et al., 2006). Combined thrusting at the base and extension at the top of the GHS played a critical role in the exhumation of the GHS.

The main goal of this research is to provide a coherent picture of how the GHS has evolved and what role the ductile, normal-sense STDS (locally known as the Zaskar

Shear Zone, or ZSZ) has played in the tectonic and metamorphic evolution of the GHS in the northwestern extension of the ZSZ in the Zaskar region. The ZSZ and the metamorphic core of the Himalaya are superbly exposed in the Zaskar region. In this study I have focused on the Suru Valley area of Zaskar. I have analyzed GHS metapelites collected in the footwall of the ZSZ using petrographic and microstructural analysis, isochemical pressure-temperature phase diagrams supplemented by geo/thermochronology data to understand the metamorphic and exhumation history of these GHS rocks in the western Himalaya.

## **2. GEOLOGIC SETTING**

The GHS, located between the STDS and the MCT, is a ~40-km-thick metamorphic sequence that contains metamorphosed sediments including high-pressure/high-temperature metapelites, metapsammities, calcareous schists, marbles, amphibolites, gneisses and quartzites (Honegger et al., 1982; Searle, 1986; Herren, 1987; Searle et al., 1992) that are intruded by and deformed along with Ordovician granites (~500-400 Ma; i.e., Mehta, 1977; Honegger, 1983; Stutz and Thoni, 1987) and undeformed Lower Miocene leucogranites (~28-14 Ma; Noble and Searle, 1995; Inger, 1998; Dèzes, 1999; Horton and Leech, 2013).

### **2.1. Regional Geology of the Zaskar Himalaya**

Three main metamorphic stages in the GHS in the Zaskar region have been described in previous studies (Kundig, 1989; Dèzes, 1999). The earliest phase ( $M_1$ ) occurred between 33 and 28 Ma at conditions of ~1 GPa and 620-650 °C (Searle et al., 1999; Walker et al., 2001). The  $M_1$  metamorphism resulted from crustal shortening and thickening during the India-Asia collision and was overprinted by a second metamorphic

phase ( $M_2$ ).  $M_2$  occurred as a result of activation of the ZSZ and MCT (Searle, 1986; Dèzes, 1999) between 22 and 14 Ma at conditions of 0.45-0.7 GPa and 650-770 °C (e.g., Searle et al., 1992; Walker et al., 1999; Godin et al., 2001).  $M_1$  mineral assemblages differ from the  $M_2$  mineral assemblages (Kundig, 1989; Searle et al., 1992) due to leucogranite generation in the GHS (Walker et al., 2001). The characteristic  $M_1$  mineral assemblage is  $Qz \pm Cld \pm Chl + Ms \pm Bt \pm Grt \pm St \pm Ky$  and the  $M_2$  mineral assemblage is characterized by  $Qz + Bt + Sil \pm Grt \pm Ms \pm Kfs$  (Kundig, 1989). The  $M_1$  and/or  $M_2$  metamorphic assemblages were overprinted by  $M_3$ , a late retrograde stage of metamorphism, which is defined by chloritization of garnet and biotite (Kundig, 1989; Sorkhabi et al., 1997). From the structurally-deepest metapelites to the structurally-shallowest rocks near the ZSZ, metapelites in the GHS show a complete succession of  $Sil/Kfs - Sil - Ky - St - Grt - Chl/Bt$  isograds ( $M_1$ ; Honegger, 1983), indicating an upward decrease in metamorphic P-T conditions (Herren, 1987; Kundig, 1989; Dèzes et al., 1999) in a typical Barrovian-type metamorphism during the early collisional stage of the Himalayan orogen (Honegger et al., 1982; Walker et al., 1999). The lowermost THS sedimentary rocks share a common protolith with the GHS metasedimentary rocks, but are separated by the ZSZ and were not buried to mid-crustal depths during early-stage thrusting on that fault (Dèzes et al., 1999). Three main deformation phases in the region were described by Walker et al. (2001): The  $D_1$  deformation phase preserves original bedding/cleavage intersections; the formation of large nappes formed the dominant  $D_2$  foliation (Walker et al., 2001); and  $D_3$  is resulted from doming and rapid mid-crustal extrusion (Searle et al., 1992; Walker et al., 2001).

The tectonic history of the ZSZ has been discussed by a number of researchers (e.g., Herren, 1987; Dèzes, 1999; Dèzes et al., 1999; Walker et al., 1999). It has been described for the first time as a synorogenic extensional fault by Herren (1985, 1987), Gilbert (1986), and Searle (1986). Estimates of vertical displacement on the ZSZ yield a minimum of  $12 \pm 3$  km (Dèzes et al., 1999). The net slip for the present-day dip of the

ZSZ (20-30°) is estimated to be between  $35 \pm 9$  km and 40-60 km by Dèzes et al. (1999) and Walker et al. (1999), respectively.

## 2.2. The Study Area: The Suru Valley in the Zaskar Region

The Zaskar Shear Zone (ZSZ) is ~150 km-long (Dèzes et al, 1999) with thickness estimates varying from 1 km to ~6.75 km (Herren, 1987; Dèzes et al., 1999; Walker et al, 1999). The Suru Valley contains the westernmost part of the GHS in the Zaskar region (Fig. 1b), and includes the towns of Rangdum, Shafat, Panikhar, Parkachik, and Sankoo from southeast to northwest, respectively (Fig. 2). Samples for this study are distributed along 80 km of the Suru River, from Rangdum to Sankoo, with the closest sample ~2-3 km from the ZSZ based on the mapped location in Searle et al. (1992), and the structurally-deepest sample is from the Suru Dome ~20 km from the ZSZ. In the southern part of the region, there is a large-scale dome called the Suru Dome. The Suru Dome resulted from  $D_3$  deformation and is a large-scale upwarp representing a late stage in the thermal history of the region (Kumar, 1995) that is associated with the  $M_2$  event of Searle and Rex (1989).

Metamorphic isograds from the chlorite-biotite to kyanite zones (Fig. 2) extend ~15 km from the ZSZ and span ~50 km along the Suru River in contrast to previous reports by numerous workers (i.e., Herren, 1987; Kundig, 1989; Searle et al., 1992; Vance and Mahar, 1998; Walker et al., 2001; Inger, 1998), and are described in detail in the next sections. The metamorphic isograds are nearly parallel to the ZSZ. The ductile ZSZ plays the main role in narrowing the isograds from an original distance of ~15 km (this study) to only 500 m in the central and eastern Zaskar (i.e., Inger, 1998) along the northern border of the GHS.

Metapelitic rocks, the main source of the data presented in this study, are abundant in the western Zaskar. Garnet, biotite, quartz, and muscovite are common

minerals along with staurolite, kyanite, and sillimanite depending on the pressure-temperature conditions and bulk-rock composition (Table 1). Ilmenite, rutile, zoisite, graphite, tourmaline, titanite, zircon, apatite, and rutile are also present as accessory minerals, mostly in the matrix, but also as inclusions in garnet.

### 3. METHODS

A large part of this research is dedicated to micro-scale observations and laboratory work to contribute to the interpretation of the tectonic, magmatic, and metamorphic history of the Zaskar region in addition to the fieldwork and macroscopic observations. I combined petrography and microstructural analysis, isochemical pressure-temperature phase modeling with *Perple\_X*, conventional thermobarometry using Fe-Mg exchange between garnet and biotite, and geo/thermochronological analysis to gain important information about the metamorphic and magmatic events which are key to understanding the geologic evolution of the area.

#### 3.1. Macrostructural Observations

From the ZSZ (Fig. 3a) towards to the Suru Dome, prograde Barrovian-type metamorphic index minerals can be clearly observed in the field as shown in Fig. 3d and Fig. 3g. Metamorphic grade increases from chlorite-biotite zone to kyanite zone in the center of the region before decreasing again southward and westward.

Non-coaxial deformation is characterized by asymmetric structures. These asymmetric structures are indicated mainly by porphyroclast systems (Fig. 3b, 3c) and recumbent folds in the Suru Valley. Recumbent folds are interpreted as premetamorphic to synmetamorphic with regards to the  $M_1$  prograde event (Walker, 2001). It is also

possible to observe the coaxial deformation defined by more symmetric structures such as in (Fig. 3b, 3e).

Structural data collected within the Suru Valley between the villages of Rangdum and Parkachik (Fig. 2) yield foliations striking ENE, dipping moderately to the NNW; lineations trend NE, plunging from  $26^\circ$  to  $56^\circ$  (Fig. 1). Mica defines the dominantly N-dipping foliation which is sub-parallel to the ZSZ and formed during extensional shearing along the ZSZ. The granitic dome that comprises the Suru Dome formed a late domal  $D_2$  foliation locally, which overprinted the  $D_1$  structures in the main part of the Suru Valley during the  $M_2$  event.

### **3.2. Petrography and Microstructural Analysis**

Thin sections were cut from sheared rocks in the footwall of the ZSZ from Rangdum to Sankoo along the Suru River; they were oriented perpendicular to the foliation and parallel to the lineation in order to deduce shear sense. Lineations are generally defined by aligned micas in metapelites that give the orientation of the stretching direction in these rocks.

Approximately thirty thin sections of Suru Valley rocks were examined by petrographic microscope to characterize mineral assemblages, and microstructures such as shear sense indicators, quartz deformation, change in general fabric with the distance to the ZSZ (i.e., size and shape of individual grains and grain boundaries), mineral inclusions, and reaction textures (see section 4.1 for results). Identifying equilibrium mineral assemblages that record P-T conditions helps constraining the prograde and retrograde metamorphic history of the studied area (see section 4.3.2). Moreover, determined mineral assemblages also helps presenting the regional distribution of Barrovian-type metamorphic isograds (see section 4.2.1) based on the presence of index minerals (chlorite, garnet, staurolite, kyanite, and sillimanite). Shear sense indicators (i.e.,

mica fish, C-S structures, C-C' shear bands, rotated porphyroblasts) preserve an important petrographic evidence to determine the direction of movement on the ZSZ. Quartz deformation and change in general fabric presents affects of the presence of the ZSZ on the GHS rocks. Mineral inclusions and reaction textures provide evidence belong to an earlier stage of the metamorphic history for constructing P-T path segments.

### **3.3. Thermobarometry and Metamorphic Modeling**

Ten representative metapelite samples were analyzed for their bulk rock chemistry using X-ray fluorescence (XRF) analysis for major and trace elements (Table 3), at the GeoAnalytical Lab at Washington State University for sample characterization and use with isochemical phase equilibrium modeling. Mineral chemistries were collected for six representative samples (Table 4) on the JEOL JXA-8230 electron microprobe at Stanford University Electron Microprobe Analysis (EMPA) Laboratory. These samples were collected at different distances to the ZSZ and the mineral chemistry data were used for Fe-Mg exchange thermometry between garnet and biotite to constrain P-T conditions of metamorphism.

The P-T history of GHS rocks in the footwall of the ZSZ can be determined using the suite of free energy minimization programs called *Perple\_X*. The programs in *Perple\_X* use bulk rock geochemical analyses, mineral chemistry analyses by electron microprobe to determine phase equilibria, modal abundance, and compositional variations within minerals to estimate P-T conditions for metamorphism. This isochemical phase equilibria modeling technique supersedes conventional thermobarometry.

### 3.3.1. Construction of Pressure-Temperature Path Segments

The isochemical phase equilibria models (i.e., pseudosections) for the Suru Valley were computed based on bulk rock XRF analysis and LOI data (used as a proxy for H<sub>2</sub>O) for samples ZH-31, ZH-34, ZH-39, ZH-43, and ZH-45 (Table 3). The *Perple\_X* models use the internally-consistent end-member thermodynamic database hp04ver.dat (ds55; Holland and Powell, 1998) with a total of seven calibrated mineral solution models: biotite (Bio(TCC); Tajcmanová et al., 2009), chlorite (Chl(HP); Holland and Powell, 1998), staurolite (St(HP); Holland and Powell, 1998), ternary feldspar (feldspar; Fuhrman and Lindsley, 1988), white mica (Mica(CHA); Coggan and Holland, 2002; Auzanneau et al., 2010), garnet (Gt(WPH); White et al., 2007), and ideal cordierite [hCrd] based on the thermodynamic database of Holland and Powell (1998). Equilibrium assemblage diagrams of each sample were calculated in a ten-component system consisting of Na<sub>2</sub>O-CaO-K<sub>2</sub>O-FeO-MgO-Al<sub>2</sub>O<sub>3</sub>-SiO<sub>2</sub>-H<sub>2</sub>O-TiO<sub>2</sub> (NCKFMASHT). These component choices ensure that most of the common rock-forming minerals in metapelites will be considered in each model (Gaidies et al., 2006). I modeled a P-T range of 0.3-1.4 GPa and 400-800 °C which is appropriate for regional metamorphism and should capture the entire P-T evolution of the rocks in the middle crust. SiO<sub>2</sub> and H<sub>2</sub>O were considered as saturated components. Ti end-members of biotite (tbi, tbit) and ilmenite (oilm, ilm\_nol) were excluded. Garnets do not show pronounced zoning and as such, XRF bulk rock powder analyses may represent a reasonable effective bulk composition. Mn was excluded due to negligible content within garnet and in bulk rock geochemical analyses (<0.2%). All pseudosections were generated as a result of these parameters (Figs. 9a, 10a, 11a, and 12a).

Compositional zoning in garnet allows further constraint of P-T paths using compositional isopleths for the grossular, pyrope, and almandine components (Ca-, Mg-, and Fe-content, respectively). The intersection of these isopleths with the P-T path estimated from pseudosection modeling defines the peak pressure where garnet growth

reached maximum pressure. As a result of these isopleths of constant chemical composition for the related samples, Figures 9b, 10b, 11b, and 12b were generated. For clarity in the models, the name of the mineral assemblages are ignored to see where isopleths intersects on the fields of stability of different equilibrium mineral assemblages. As a result of this combination, Figures 9c, 10c, 11c, and 12c were generated.

Next step to constraint the P-T path is calculation of maximum metamorphic temperatures using garnet-biotite Fe-Mg exchange thermometry (Ferry and Spear, 1978; Hodges and Spear, 1982) with garnet core and rim chemistries (Table 4). Samples reached maximum temperatures on the retrograde part of the P-T path which is estimated to be the average of these two thermometer calibrations. As a result of these calibrations, Figures 10d, 11d, and 12d were generated with the data from previous steps of generating P-T path.

The prograde history of Zanskar rocks is difficult to decipher because garnets do not always show pronounced zoning between rim and core (see Table 4). Furthermore, even if garnets belongs to this study had strong zoning, it would not be possible to generate the P-T path of the first ~20 km of burial assuming garnet begins growing at pressures of 0.6-0.7 GPa (Vance and Harris, 1999; Walker et al., 2001). Vance and Mahar (1998) constrained the pressure for the beginning of garnet growth at 0.3-0.7 GPa. For these reasons, only peak pressures, peak temperatures, and retrograde phase in pseudosection models were calculated for four rocks studied based on results from petrographic and geochemical analyses, and comparisons to conventional thermometry.

### **3.4. Geochronology**

Zircon U-Pb geochronology was used to determine the timing of metamorphism or granite crystallization based on the closure temperature of zircon (>700 °C; Spear, 1993). U-Pb depth-profiling analyses of zircons from three metapelite samples were

conducted in the U.S. Geological Survey and Stanford University SHRIMP-RG (SUMAC) facility at Stanford University (Table 5), to constrain the age of metamorphism during the Himalayan orogeny.

Zircon age standard Temora-2 (416.8 Ma; Black et al., 2004) and an in-house compositional standard (MADDER) were co-mounted with unknown zircons. Standard grains were pressed into soft indium metal held in a 25-mm-diameter, 5-mm-thick aluminum disk, which was then ground and polished to a 1-micron finish. Unknown zircon grains, concentrated by standard heavy mineral separation processes, were hand selected and mounted on glass slides coated in a thin (<10 microns) film of vacuum grease. This grease allows the grains to be easily manipulated and arranged in  $\sim 1 \times 6$ -mm rows with the flat euhedral zircon surfaces (m-face) oriented down, against the glass. Oriented zircon grains were pressed into the pre-polished indium, exposing flat non-polished zircon surfaces parallel with the mount surface and standard grains. Three mounts (ZH-1 and ZH-2) were created and zircon U-Pb ages were measured over three, two-day sessions.

All grains were imaged with reflected light on a petrographic microscope, and Temora-2 with cathodoluminescence (CL) on a JEOL 5600 SEM to identify internal structure, inclusions, and physical defects. The mounted grains were submerged in acetone to remove mounting grease, scrubbed with soap and water, rinsed in dilute ethylenediaminetetraacetic (EDTA) acid and distilled water, dried in a vacuum oven, and coated with  $\sim 100 \text{ \AA}$  Au. The mounts were stored at high pressure ( $10^{-7}$  torr) for several hours before being moved into the source chamber of the SHRIMP-RG to minimize degassing of the epoxy and isobaric hydride interferences and masses 204-208.

Secondary ions are generated from the target spot with an  $\text{O}_2^-$  primary ion beam varying in intensity from 2.5 to 3.5 nA. The typically primary ion beam was defocused to achieve a flat-bottomed pit 20-25 microns in diameter and  $\sim 1.3$  to 1.5 microns deep,

measured using Zygo® NewView7200 interferometer at University of California, Santa Cruz. The Au was removed from the sample surface by pre-sputtering the primary beam for 30 seconds before data were collected. Measurements were made at mass resolutions of  $M/\Delta M = 8000-8500$  (10% peak height), which eliminates interfering molecular species. The acquisition routine included high-mass normalizing species ( $^{90}\text{Zr}^{16}\text{O}^+$ ), followed by  $^{180}\text{Hf}^{16}\text{O}^+$ ,  $^{204}\text{Pb}^+$ , a background measured at 0.046 AMU above the  $^{204}\text{Pb}^+$  peak,  $^{206}\text{Pb}^+$ ,  $^{207}\text{Pb}^+$ ,  $^{208}\text{Pb}^+$ ,  $^{238}\text{U}^+$ ,  $^{232}\text{Th}^{16}\text{O}^+$ , and  $^{238}\text{U}^{16}\text{O}^+$ . All peaks were measured on a single EPT® discrete-dynode electron multiplier operated in pulse counting mode. Each mass was counted for 2, 1, 2, 10, 20, 10, 1, 5, 2, 4 seconds, respectively, with emphasis placed on measuring  $^{206}\text{Pb}$ ,  $^{207}\text{Pb}$ , and  $^{238}\text{U}$ . Because the U-Th concentration and age can change as the analysis depth profiles increase with time, we attempted to analyze  $^{206}\text{Pb}$  and  $^{238}\text{U}$  as close together in time as possible to avoid mixing different domains.

All analyses were performed with 5 scans by peak-hopping from mass 195.8 through 254. The primary focus was measuring ages from zircon rims, which can be  $<1$   $\mu\text{m}$  thick, based on measurements by interferometry of zircon crystals. Results presented here and by previous workers (e.g., Noble and Searle, 1995; Horton and Leech, 2013; Finch et al., 2014) have shown that Zanskar zircons contain relatively high-U Miocene rims and Permian and/or Proterozoic and Early Paleozoic cores. The large age difference between zircon domains allows us to easily distinguish between U/Pb ratios of young overgrowths, relative to older protolith/xenocrystics core ages. The boundary between these zircon domains is sharp based on backscatter electron and cathodoluminescence imaging, and U-Pb dating of different zircon domains in this and previous studies (e.g., Horton and Leech, 2013); any mixing during depth-profiling through zircon rims is clear because of this large age difference between the zircon rims and cores (i.e., rather than long episodic or continuous growth that would result in ages becoming steadily older). Therefore, for individual analyses for which the age increased more than  $\sim 20$  Ma over the 5 cycles of data acquisition (i.e., depth profiling into an older age domain with depth),

only the youngest 2, 3, or 4 cycles were used to calculate rim ages. To determine whether the young ages were in fact representative of the rim ages, or whether the calculated ages were biased as a result of depth profiling, four zircon grains that indicated young ages based on 5 cycles data were reanalyzed using a  $\sim 1.5$  nA beam current and a 20-25 microns diameter by  $\sim 1.5$  to 1.8 microns deep spot. The run table was the same as above, but with  $^{197}\text{Au}$  added after HfO. Each mass was counted for 1, 0.5, 1, 0.5, 0.5, 8, 6, 1, 3, 2, and 3 seconds, respectively. These analyses decreased the sputter rate and increase the depth resolution of the analysis by a factor of 9, but increased the analysis time from approximately 20 to 65 minutes. The 45 cyclers analyses reveal that depth-profiling yields the same age as 5 cycle analyses, and is reproducible over ten's of cycles. It also reveals that the largest source of analytical uncertainty (particularly for the  $^{206}\text{Pb}/^{238}\text{Pb}$  ratio) in the 5 cycle analyses is from mixing and averaging between zircon zones that vary in the U, Th, and Pb over 0.05-01 micron depths, or when sputtering into older cores. Common Pb contamination accounts for a smaller, secondary source of error.

U-Pb ages determined by SIMS are reliant upon the assumption that the standards are treated in the same manner as the unknowns. Therefore, the data was reduced using two methods: (1) the U-Pb calibration constant was calculated using 5 cycles of Temora-2 data for unknown analyses that yielded Tertiary ages from 4 or 5 cycles, or (2), for analyses in which only 2 or 3 cycles yielded Tertiary ages, the U-Pb calibration constant was calculated using 3 cycles of Temora-2 data. The calibration constant for Temora-2 calculated using 3 versus 5 cycles differed by 1.28%. Given the 1-2% uncertainty in the ages of individual analyses, the calculated model ages are insensitive to the treatment of standard data, and much more sensitive to variations in the  $^{206}\text{Pb}/^{238}\text{U}$  and U-concentrations with depth. Zircon concentration data for Hf, U, and Th are standardized against well-characterized, homogeneous in-house zircon standards MADDER (3435 ppm U, calculated relative to MAD-green (Barth and Wooden, 2010).

Calculated model ages for zircon are standardized relative to Temora-2, which were analyzed repeatedly throughout the duration of the analytical session (every 4<sup>th</sup>

analysis). Data reduction for geochronology followed the methods described by Williams (1997) and Ireland and Williams (2003), and used the MS Excel add-in programs Squid2.51 and Isoplot3.76 of Ludwig (2009; 2012). The measured  $^{206}\text{Pb}/^{238}\text{U}$  was corrected for common Pb using  $^{207}\text{Pb}$ . The common-Pb correction was based on a model Pb composition from Stacey and Kramers (1975). All reported  $^{206}\text{Pb}/^{238}\text{U}$  and  $^{207}\text{Pb}/^{206}\text{Pb}$  model ages and uncertainties ( $2\sigma$ ) include error summed in quadrature from the external reproducibility ( $1\sigma$  SD) of the standard Temora-2 during an individual analytical session (16-24 hours). To mitigate bias caused by the depth profiling through zircon zines that differ in U, Th, Pb, or age; analyzed grains were systematically excluded from these calculation if their  $1\sigma$  errors were greater than 10% of the  $^{206}\text{Pb}/^{238}\text{U}$  calculated ages as were analyses with errors  $>15\%$  for the total  $^{206}\text{Pb}/^{238}\text{U}$  count. Some grains that did not meet these criteria were still included when there were a small number of grains analyzed to decrease the error in the calculated age, thereby strengthening the quality of the age calculation. The intercept ages for Terra-Wasserberg diagrams are all calculated with a  $^{207}\text{Pb}/^{206}\text{Pb}$  ratio of 0.837 (Fig. 15). This anchored projection line also provides a common reference frame for sample-to-sample comparisons.

## 4. RESULTS

### 4.1. Microstructural Evolution

Petrographic analyses were completed for rocks along the Suru Valley to relate regional prograde Barrovian-type and retrograde metamorphic events to deformation events. This valley is oriented SE-NW from Rangdum to Tongul in the Suru Dome, and S-N from Tongul to Sankoo along the Suru River. The ZSZ is exposed just west of Rangdum in the eastern side of the Suru Valley and immediately south of Sankoo in the northwestern part of the valley (Figs. 1, 2). In addition to field observations, the textural transition between samples (both samples from Horton and Leech, 2013) Z-27

(sedimentary, THS) and Z-34 (metamorphic, GHS) indicates that the ZSZ should be located not more than 3.5 km west of Rangdum. This distance indicates that the thickness of the ZSZ should be  $\leq 3.5$  km, corresponding to the estimates of 1-2 km for the ZSZ suggested by Dèzes et al. (1999) and Walker et al. (1999).

Macro- and microscale shear sense indicators and deformation mechanisms vary based on distance from the ZSZ. Mineral “fish” are a ductile shear sense indicator, and a number of minerals (most commonly micas) develop as mineral fish oriented in a mylonitic foliation (Passchier and Trouw, 2005). Mineral fish are not a common shear sense indicator in samples collected for this study compared to Mukherjee and Koyi (2010); lenticular mica fish (Fig. 4d) and parallelogram-shaped mica fish (Figs. 4a, 4b), are present in sample ZH-33. Additionally, a lenticular garnet fish (Fig. 5b), parallelogram-shaped garnet fish (Fig. 5e) are found in samples ZH-33 and ZH-39, respectively, although garnet fish are rare in general. These mineral fish in Zanskar rocks show either a top-to-the-SW or a top-to-the-NE shear sense. Also present are C-S structures and  $C'$ -type shear bands as shear sense indicators. Sample ZH-33 from the Rangdum-Shafat area in the garnet zone displays a typical  $C'$ -type shear band that developed late in the ZSZ activity and overprints a C-S fabric (Fig. 4c).  $C'$ -type shear band in C-S fabric which is parallel to shear zone boundaries shows a top-to-the SW thrusting.

In addition to seeing these fabrics in the micaceous matrix, mineral inclusions contain significant information of an earlier stage in the metamorphic history. As shown in Fig. 6c, S fabric shows an earlier foliation in micaceous minerals preserved as inclusions in other minerals. The same figure also records mineralogical evidence of the order of mineral nucleation and growth; specifically, first biotite, then titanite, and lastly staurolite. A similar record of mineral growth is preserved elsewhere in the same sample which shows that first tourmaline, titanite, and then staurolite grew (Fig. 6d).

Rotated objects such as garnet porphyroblasts record evidence of shear sense in addition to preserving different stages of foliation development. Most of the garnets are wrapped by biotite and muscovite as seen in the Figure 5b, 5d and 5e. Garnet poikiloblasts from ZH-33, -34, -39, and -43 present either a top-to-the-SW or a top-to-the-NE shear sense (Fig. 5). Fig. 5f also shows that the zoning pattern in a snowball garnet from sample ZH-43 in the Suru Dome records more recent top-to-the-NE motion on the ZSZ. Horton and Leech (2013) also document a snowball garnet (Z-40) that also shows top-to-the-SW shear sense. These microtextural observations indicate that thrusting and normal shearing must be coplanar and codirectional.

Microstructural studies are important to understand the crustal flow mechanisms and deformation patterns in shear zones. This study also focuses on quartz because it is common and forms well-defined textures that can be linked to micro-scale deformation mechanisms that occur in ductile shear zones, even at relatively low temperatures (over  $\sim 300$  °C). Reduced grain size of quartz (Fig. 8) results from dynamic recrystallization during shearing. Two main types of dynamic recrystallization are observed in the ZSZ: subgrain rotation (SGR) and grain boundary migration (GBM). Newly-crystallized grains tend to be much smaller at lower temperatures (250-300 °C) and/or fast strain rates (Vernon, 2004). SGR is observed in sample ZH-31 from the garnet zone (Fig. 7a) while GBM is indicated by irregular grain boundaries and occurs throughout most of the area as shown in sample ZH- 3 (Fig. 7b). Each of these recrystallization mechanisms is active within a specific temperature range, though quartz textures may be affected by mineralogic heterogeneity within these rocks. The dominant recrystallization mechanism by SGR occurs at 400-500 °C, while GBM takes place between 500 and 700 °C (Stipp et al., 2002; Passhier and Trouw, 2005). However, quartz microtextures do not depend solely on the temperature of deformation, but also strain rate, differential stress, and the presence of water (Passhier and Trouw, 2005). The effects of the dynamic recrystallization of quartz grains can also be seen with the change of quartz grain size that increases from 0.05 to 2 mm with increasing distance from the ZSZ. Additionally of note

is that there is a significant change for the size of micaceous minerals as well. The shape of individual quartz grains also indicates deformation mechanisms: quartz grains vary from elongate, anhedral grains with interlobate grain boundaries near the ZSZ to euhedral grains from the Suru Dome. The change in size distribution of grains is another remarkable feature. Taken together, the distance to the ZSZ effects quartz grain size, shape, the grain form, and the size distribution of grains in a general trend.

Additionally, it is possible to see the fabrics belonging to early stages of metamorphism better at higher structural levels close the ZSZ footwall rather than the rocks from the Suru Dome. Suru Dome rocks record a different fabric, with coarser grains and large sheaves of mica minerals defining a spaced foliation as described by Searle et al. (1992) (Fig. 8). The index minerals for Barrovian-type metamorphism, staurolite, kyanite, and sillimanite, overgrow the earlier fabric and are aligned along the main foliation. The transition between these zones will be discussed further below.

## **4.2. Metamorphic History**

Both prograde regional metamorphism and retrograde metamorphism are recorded by metapelites in the study area. A complete succession of prograde Barrovian-type metamorphism occurs, increasing from chlorite-biotite grade to kyanite grade, progressively and across only ~15 km from the THS into the GHS in the footwall of the ZSZ. Retrograde metamorphism is defined by the appearance of new minerals such as sillimanite, and cordierite.

### **4.2.1. Prograde Metamorphism and Metamorphic Isograds**

The occurrence of Barrovian index minerals depends largely on the bulk composition of the rocks and the metamorphic grade (Spear, 1993; Walker et al., 2001).

The regional distribution of metamorphic isograds in the Zaskar region was replotted with the new data of this study (Fig. 2) because petrographic analyses and field observations of the appearance of index minerals in metapelites disagreed with the isograd maps proposed by Herren (1987), Kundig (1989), Inger (1998), Searle et al. (1999), Walker et al. (2001), and Noble et al. (2001). The contradictions are both in the nomenclature and location of the isograds; the isograd map in this study was created based on the samples collected only along the Suru River. Therefore, the locations of the isograds in the mountainous region north of the Suru Valley are approximate. Additionally, the samples collected between the location of sample ZH-43 near Panikhar and the ZSZ on the western side of the Suru Valley do not support the continuity of the isograds because the index minerals are not present. Thus I assumed the isograds are approximately parallel to the ZSZ as shown by other workers.

Several studies suggest that there is a succession of Barrovian index minerals in Zaskar (i.e., Herren, 1987; Kundig, 1989; Inger 1998; Dèzes et al., 1999; Searle et al., 1999; Walker et al., 2001; Noble et al., 2001), but these studies do not include the lowest-grade chlorite zone. Petrographic evidence in Z-34 indicates prograde/peak Barrovian chlorite growth (Fig. 4e), which differs from all other samples along the Suru Valley that include retrograde chlorite (see also Searle et al., 1999). This chlorite is considered to be a result of prograde metamorphism in the ZSZ in Suru Valley due to the distance from the ZSZ, but because it co-exists with biotite I have labeled this the chlorite-biotite zone (Fig. 2). The garnet zone is represented by sample ZH-31 which does not contain biotite based on petrographic and mineral chemistry analyses (Figs. 6a, 6b). Therefore, the location of this sample should mark the garnet-in isograd and should not be labeled the garnet-biotite zone as in several studies (Herren, 1987; Kundig, 1989; Inger, 1998; Searle et al., 1999; Walker et al., 2001). This places the garnet-in isograd much closer to the chlorite-biotite isograd compared to previous studies. The location of samples ZH-34 and ZH-35 have previously been placed in the staurolite zone, but those samples do not contain staurolite; it is possible that the bulk chemistry of samples ZH-

34 and ZH-35 does not contain sufficient Mg to crystallize staurolite, but it is nevertheless expected in the host rocks. The sample ZH-36 is the representative one for the staurolite isograd. The kyanite zone is not shown in Herren (1987), Kundig (1989), Staubli (1989), Inger (1998), and Vance and Mahar (1998) suggesting these authors did not observe kyanite and interpreted Zanskar rocks to have experienced lower-pressure and/or higher temperature metamorphism. Kyanite is clearly present (see Fig. 5e) and is supported by several reports (Searle and Rex, 1989; Walker et al., 2001; Noble et al., 2001). I observed the first appearance of kyanite near Parkachik in the southeastern part of the Suru Dome which contradicts these earlier studies. These earlier studies also place the sillimanite+k-feldspar isograd on the southeastern side of the Suru Dome. In this study, sillimanite only occurs with orthoclase in the Suru Dome along with muscovite, biotite, and chlorite that grew during retrograde metamorphism (Fig. 5d). There is no way to distinguish the sillimanite-muscovite zone from the sillimanite-K-feldspar as proposed in many studies (i.e., Walker et al., 2001) because sillimanite-K-feldspar-muscovite occur in the same sample from the Suru Dome (ZH-41).

Table 1 gives the mineral assemblages for representative samples along with location names and coordinates. There is a typical high-temperature/high-pressure, Barrovian-type metamorphic field gradient, condensed to an approximately 15 km-thick sequence in the Suru Valley. The successive prograde assemblages and the related metamorphic isograds from the lowest to highest grade (Chl-Bt, Grt, St, Ky, respectively) within the ZSZ are described below.

### ***The Chlorite - Biotite Zone***

Chlorite-biotite zone in the study area is represented by sample Z-34 near Rangdum and nearest to the ZSZ (Fig. 4e). Based on microtexture in sample Z-34, this metapelite was deformed within the ZSZ, and Z-34 is the only sample collected from

within the main shear zone. Based on the location of Z-34 relative to other samples, it defines the ZSZ as only a ~1-km-thick zone in the northern part Suru Valley (Dèzes et al., 1999; Walker et al., 1999). This differs from the central and eastern part of the Zanskar region, exemplified by Sumche Tokpo, Lechan Tokpo, Malung Tokpo where metamorphic isograds are condensed in a 200- to 250-m-thick mylonitized zone comprising the ZSZ (i.e., Herren, 1987; Dèzes et al., 1999). Epidote minerals in this sample are observed as a replacement in porphyroblasts with pressure shadows. The very fine-grained phyllite from this zone consists of the assemblage of Qz + Chl + Cld + Bt + Ms + Ep + Rt (Tables 1, 2). The foliation is defined by the preferred orientation of chlorite, chloritoid, and biotite. Chlorite is also present in all other zones as a retrograde mineral; mainly garnet and biotite are transformed to chlorite as also mentioned in Epard and Steck (2004).

### ***The Garnet Zone***

The type of rocks in the garnet zone changes from phyllite to schist. The garnet zone starts within ~2 km to the south of the chlorite zone (Fig. 2) with phyllite sample ZH-31. Searle et al. (1992) divided schists into two textural types denoted as Type 1 and Type 2 based on textural properties such as the presence of graphite in Type 1 schists. However, because only one sample (a phyllite, ZH-31) included in this study contains graphite (Figs. 6a and 6b), and some of the textural properties such as garnet breakdown in the Suru Dome area are not observed (Searle et al., 1992), I do not categorize samples similarly in this study. Garnet porphyroblasts are up to 5 mm, and are larger in this sample as compared to other zones. Some garnet porphyroblasts are partially replaced by chlorite, muscovite, and graphite. Although a typical mineral assemblage for this zone is  $\text{Grt} + \text{Chl} + \text{Ms} + \text{Qz} + \text{Tur} + \text{Rt} \pm \text{Bt} \pm \text{Ilm} \pm \text{Gr} \pm \text{Ap}$ , biotite is absent in sample ZH-31 which exhibits a mylonitic texture containing felsic (Qz + Pl) and micaceous (Bt + Ms) layers. Garnet porphyroblasts indicating  $M_1$  metamorphism are generally wrapped by

micaceous layers exhibiting an  $S_2$  foliation that developed during SW-directed thrusting (Fig. 5). Finch et al. (2014) defines garnets only with inclusion trails, but there are several examples of the garnets without inclusion trails such as Fig. 5c that likely indicates a pre-tectonic episode. Pre-tectonic porphyroblasts are rare in Barrovian metamorphic mineral assemblages, apart from the possible existence of low-pressure/high-temperature metamorphic minerals. Asymmetrical strain shadows in the matrix foliation are observed with both straight and helitic inclusion trails; these inclusion trails contain mostly matrix minerals of  $Qz \pm Pl \pm Bt \pm Ms$  and rarely  $Rt \pm Zo \pm Opq$ . Inclusions are much smaller than those in the matrix as a result of dynamic recrystallization during deformation. Garnets are present in almost all samples in the studied area, apart from the chlorite-biotite zone rocks.

### *The Staurolite Zone*

Rocks in the staurolite zone are coarser grained than those in the garnet zone. The typical mineral assemblage for this zone is  $Qz + Bt + St + Grt + Ms \pm Pl \pm Chl \pm Crd \pm Ilm \pm Rt \pm Ttn \pm Tur \pm Zrn$  (e.g., sample ZH-36; Figs. 6c, 6d). Most of the staurolites have inclusions of biotite and quartz. The main foliation is defined by aligned biotite and muscovite, and most staurolite grains are elongate parallel to the main foliation. This zone is narrower than both the garnet and kyanite zones, and Dèzes (1999) interpreted this to be a small temperature window at 30 °C in the MnKFMASH system due to the reaction of  $Grt + Chl = St + Bt + H_2O$  and  $St + Chl = Bt + As + H_2O$  within the above typical mineral assemblage. Staubli (1989) also mentions this narrow staurolite zone in the Kishtwar window near the MCT in the southern part of the study area (Fig. 1), due to a Fe-Mg-rich but Al-poor bulk composition hindering nucleation, or breakdown reactions, during late-stage metamorphism. However, staurolite porphyroblasts are abundant in both staurolite and kyanite zones.

### *The Kyanite Zone*

The kyanite zone is located in the southwest part of the study area, and is represented by sample ZH-37 from near Parkachik in the Suru Dome. Kyanite grew during prograde regional metamorphic event ( $M_1$ ), contrary to Kundig (1989). Elongate kyanite grains are parallel to the main foliation (Fig. 5e) that is also defined by aligned biotite and muscovite. A typical mineral assemblage for kyanite zone zone is  $Qz + Bt + Ms + St + Grt + Ky \pm And \pm Sil \pm Alb \pm Chl \pm Tpz \pm Zo \pm Di \pm Ilm \pm Tur \pm Rt$ . Dèzes et al. (1999) states that the kyanite zone is identified by the appearance of kyanite and the disappearance of chlorite, however kyanite zone rocks include chlorite as a retrograde mineral. Samples from this zone differ from Staubli (1989) in that kyanite does not appear as inclusions within garnets nor does kyanite contain inclusions. Sillimanite is also found in sample ZH-41 from the kyanite zone. Because K-feldspar and sillimanite are a result of a retrograde metamorphism, I consider this part of the kyanite zone rather than defining the Sil-in isograd.

#### **4.2.2. Retrograde Metamorphism**

The GHS rocks undergo a later retrograde metamorphism during decompression, and defined by the appearance of new metamorphic minerals such as sillimanite, cordierite, k-feldspar, and andalusite in that order. These minerals suggest a retrograde path starting with a more or less isothermal decompression, and followed by more pronounced cooling (Dèzes et al., 1999). Chlorization of garnet, biotite, and staurolite is typical for a late-stage of this phase.

The appearance of sillimanite is the first indicator of retrograde metamorphism. Only fibrous sillimanite (fibrolite) is found in the Suru Valley; coarse-grained, prismatic sillimanite appears only in the southeastern part of the region. There is no petrographic evidence that fibrolite in sample ZH-41 replaces kyanite; it grows on the C/S fabrics (Fig.

6e) that indicate an extension-induced decompression (Dèzes et al, 1999). Fibrolite forms either from biotite breakdown or less commonly by the overgrowth of muscovite as also indicated in Staubli (1989). Although rutile is one the most abundant accessory minerals in most samples, it is not present in ZH-41. Instead, fibrolite coexists with small prisms of ilmenite recrystallizing from the Ti released during biotite breakdown to fibrolite (Staubli, 1989). In the literature, the sillimanite isograd is shown east of the Suru Dome (e.g., Sorkhabi et al., 1997), but this study suggests that sillimanite is present in the Suru Dome. The sillimanite isograd should therefore cross the Suru Dome around Tongul and continue to the southeastern part of the region. However, recall that the sillimanite zone is not shown because Fig. 2 is mapped based on prograde Barrovian-type metamorphism. Additionally, there is no other sample from the study area that allows connecting the two locations of sillimanite-bearing rock locations to create the related isograd.

Cordierite appears in both the kyanite zone and staurolite zones. The appearance of k-feldspar porphyroblasts (~7 mm) with small-scale quartz minerals indicate incipient partial melting, but the existence of muscovite also shows that the P-T conditions reached did not induce pervasive melting as stated in Dèzes et al. (1999).

Andalusite porphyroblasts are larger than any kyanite examined in the thin sections, and there is no petrographic evidence that andalusite replaces kyanite. Andalusite is not reported in the literature for the Zanskar region except in Dèzes (1999) and Epard and Steck (2004). The sample ZH-41 from the Suru Dome is a good example suggesting a retrograde metamorphism by tectonic decompression during the ZSZ extension because it has coexistence of these four retrograde minerals in the kyanite zone.

### 4.3. Quantitative Pressure-Temperature Paths

#### 4.3.1. Mineral Chemistries

Garnet compositions were analyzed in five samples (ZH-31, -34, -39, -43, and -45) by electron microprobe for use in isochemical phase modeling using the program *Perple\_X* (Table 3). The garnets analyzed in this study show varying degrees of compositional zoning, but zoning is generally weak or absent. Garnets that do show zoning display a normal prograde-type zonation. Mn is generally higher in the cores of garnets and the Mg content increases at the rim either at the expense of Ca, Mn, or both. The Fe content is variable, either increasing or decreasing slightly towards the rim of the garnet.

The grossular component ( $\text{Ca}/(\text{Fe}+\text{Mg}+\text{Ca}+\text{Mn})$ ) depends on the sample, with maximum Grs = 0.20 to 0.22 and a minimum Grs = 0.04. Almandine ( $\text{Fe}/(\text{Fe}+\text{Mg}+\text{Ca}+\text{Mn})$ ) is the dominant component with values ranging from 0.63 to 0.76. Pyrope contents ( $\text{Mg}/(\text{Fe}+\text{Mg}+\text{Ca}+\text{Mn})$ ) vary from 0.05 to 0.16. A few garnets have spessartine components ( $\text{Mn}/(\text{Fe}+\text{Mg}+\text{Ca}+\text{Mn})$ ) as high as 0.12 in the cores, but most grains range from 0.02 to 0.05.

Biotite is pervasive throughout all samples except the sample ZH-31. Tetrahedral Al ranges from 1.20 to 1.34 apfu in matrix biotite without zonation. The octahedral Al content is noticeably higher in the rims of matrix biotite, ranging from 0.39 to 0.45, compared to 0.47 to 0.55 in the cores.  $X_{\text{Mg}}$  varies from 0.53 to 0.58 with the exception of sample ZH-34 which contains biotite with higher a Fe component ( $X_{\text{Mg}} = 0.34$  to 0.37). All analyzed matrix white mica indicates little phengite ( $\text{SiMg}/(\text{AlAl})$ ) or paragonite ( $\text{Na}/\text{K}$ ) substitution, and are nearly ideal muscovite. The tetrahedral Al content in muscovite ranges from 0.95 to 0.99 apfu and Na contents are  $<0.09$  apfu. Plagioclase compositions are Na-rich with  $X_{\text{Ca}} < 0.20$  (Table 4).

### 4.3.2. Pressure-Temperature Constraints

The calculated pseudosections for samples ZH-31, -34, -39, and -43 (Figs. 9a, 10a, 11a, 12a, respectively) allow only interpretation of the peak and retrograde stage of the metamorphic evolution of metapelites from the Zanskar region. Recall that lack of garnet zonation does not allow creating an early stage of retrograde path. The model for ZH-45 is not included in this study because of difficulties generating an interpretable pseudosection, likely due to retrogression. However, mineral composition of the sample is presented in Table 4. It is also not possible to suggest a complete P-T path for sample ZH-31 because of the absence of biotite prevents determining peak temperature using garnet-biotite Fe-Mg exchange thermometry as mentioned above. However, the peak pressure of this garnet zone sample is constrained at  $\sim 1.18$  GPa and  $\sim 550$  °C (Fig. 9c) with the peak mineral assemblage of Chl + Ms + Pr + Grt + Ilm + Qz (Fig. 9a, Table 2). Mineral chemistry data for ZH-31 is included in Table 4. Mineral inclusions (Fig. 6c, 6d) and reaction textures (Fig. 4e, 6e) preserving early stage of the metamorphic history in addition to mineral assemblages help in determining the trajectory of the P-T path. Therefore, all the mineral assemblages on the constrained P-T path should be consistent with the petrographic data.

Pseudosection modeling of sample ZH-34 from the garnet zone using a SiO<sub>2</sub>- and H<sub>2</sub>O-saturated NCKFMASHT system, the peak mineral assemblage of Bt + Ab + Ms + Grt + Ilm + Qz is stable at  $\sim 1.23$  GPa and  $\sim 590$  °C (Fig. 10; Table 2). The models for samples ZH-39 and ZH-43 both from the kyanite zone, using the same thermodynamic system and peak mineral assemblages of Bt + Ab + Ms + Pg + Grt + Rt + Qz and Bt + Ab + Ms + Grt + Rt + Qz, respectively, give similar pressures of  $\sim 1.10$  GPa at 620 °C and  $\sim 1.10$  GPa at 630 °C, respectively (Figs. 11, 12, respectively; Table 2). After peak pressure conditions were reached, there was an isothermal decompression period before final exhumation. Peak temperatures for samples ZH-34, -39, and -43 reached  $\sim 620$  °C,  $\sim 700$  °C, and 640 °C, respectively (Figs. 10d, 11d, 12d). Among these results, the

temperature of  $\sim 700$  °C is more than expected for a sample from the kyanite zone. However, as can be seen in Figure 11, pressure is greater than 1 GPa. Therefore, it may not be possible for this sample to stabilize sillimanite under these conditions, but also with the mineral composition it contains. On the other hand, the location of this sample collected is from the Suru Dome which occurred as  $M_2$  event associated with crustal anatexis (Walker, 2001) evidenced by generation of leucogranites and equilibration of the minerals (Searle et al., 1992; Walker, 2001).

Overall, these modeled P-T paths are consistent with most of the textural and compositional features found in the samples, and they all experienced a common, clockwise regional metamorphic path. The P-T modeling of the rocks from different isograds shows that the peak pressure is greater than 1 GPa at  $\sim 550$ - $630$  °C and peak temperature is varying  $620$ - $700$  °C. Peak temperatures are at their maximum in the Suru Dome as expected due to existence of sillimanite in the area. On the other hand, the peak pressure of different samples is slightly decreasing (see the comparison in Fig. 13) from the ZSZ towards the Suru Dome due to doming occurred as a later event ( $M_2$ ) as described in Walker (2001).

#### **4.4. U-Pb Zircon Geochronology**

U-Pb SHRIMP depth-profiling analyses of zircon were performed to constrain the phases of high-grade metamorphism on Suru Valley metapelites. Zircon was chosen for analysis because of its high, relative closure temperature  $>700$  °C (Heaman and Parrish, 1991; Spear, 1993), which is appropriate for peak temperature because it is close to, but does not exceed the liquid solidus.

Three samples distributed SE-NW along the Suru River from Rangdum to Tangol were analyzed for zircon U-Pb geochronology (Fig. 15) and results are summarized below. Only grains that we were confident reflected the age of Miocene are presented

here as reported by Noble and Searle (1995), Dèzes et al. (1999), Walker et al. (1999), Leech (2008), Horton and Leech (2013), Finch et al. (2014). Older ages of Proterozoic zircon interiors have been presented in Horton and Leech (2013), and mixed ages that capture rim and interior zones are geologically meaningless and not reported here. Previous dating studies in the Zanskar region are summarized in sections of 5.2 and 5.3.

*Z-32: Garnet schist*

This is a highly deformed garnet schist from the village of Jildo near Rangdum (Fig. 2). U-Pb depth-profiling analysis captured the Miocene history of three zircon grains for this study, recording an average age of  $17.2 \pm 5.3$  Ma. This same sample was previously analyzed by Laser Ablation Inductively Coupled Mass Spectrometry (LA-ICP-MS), and six zircon grains gave 1100-995 Ma ages from interior zircon domains recording inheritance from the protolith (Horton and Leech, 2013).

*ZH-36: Staurolite garnet schist*

The main foliation is defined by mica minerals in this porphyroblastic schist from between Shafat and Parkachik (Fig. 2). Eight zircon grains from ZH-36 provide a mean age of  $21.6 \pm 2.7$  Ma.

*ZH-41: Kyanite sillimanite schist*

This high-grade schist from near Tongul in the Suru Dome that contains garnet porphyroblasts that have only curved inclusion trails. Nine zircon grains from this sample (ZH-41) yield an average age of  $19.9 \pm 0.9$  Ma.

## 5. DISCUSSION

### 5.1. Metamorphic Implications of the Zaskar Region

The pressure-temperature constraints for Greater Himalayan rocks have been discussed in detail by several workers (e.g., Searle et al, 1992; Vance and Mahar, 1998; Dèzes et al, 1999; Searle et al, 1999; Vance and Harris, 1999; Walker et al, 1999; Walker et al, 2001; Finch et al, 2014). There is a general agreement that temperature increases from the ZSZ through to the Suru Dome based on the appearance of index minerals, and confirmed by my pseudosection modeling. Pressure increases with structural depth beneath the ZSZ with the exception of the Suru Dome which experienced metamorphic re-equilibration during a late doming event.

Searle et al. (1992) estimated average P-T conditions of 650-700 °C at ~0.8 GPa for Suru Dome rocks, using the dataset of Holland & Powell (1990); they calculate a burial depth of 28-30 km assuming a lithostatic gradient of 3.5-3.7 km/kbar. Vance and Mahar (1998) calculated 550 °C and 0.3-0.7 GPa from garnet cores and 650-700 °C and 0.9-1.1 GPa from garnet rim data in semipelitic/pelitic schists from different structural depths in the Suru Valley using THERMOCALC (Powell and Holland, 1988). Vance and Mahar (1998) also report that decompression after garnet growth was rapid due to isostatic rebound that was followed by fairly rapid cooling. Dèzes et al. (1999) used different thermobarometers to study metapelites from SE Zaskar and suggested that both temperature (550-700 °C) and pressure (0.59-0.91 GPa) increase gradually from the biotite zone to the kyanite zone that contains retrograde fibrolitic sillimanite. Searle et al. (1999) reported a slightly different P-T range of 550-680 °C and 0.95-1.05 GPa for kyanite-grade rocks from the Suru Valley (including Suru Dome), and 650-770 °C and 0.45-0.7 GPa for sillimanite-grade rocks near Shafat using THERMOCALC. Based on the same samples from Vance and Mahar (1998), Vance and Harris (1999) state that

heating and burial to 0.6-1.0 GPa at a peak temperature of ~700 °C caused crustal melting at 24-18 Ma without an additional heat source, and likely as a result of rapid decompression and the breakdown of muscovite. Walker et al. (1999) describes peak metamorphic conditions for pelitic schist samples from the garnet and/or staurolite zone(s) in the footwall of the ZSZ of 0.6-0.8 GPa and 550-650 °C. Walker et al. (2001) built on their earlier work using combined THERMOCALC and GIBBS on pelitic samples from the Suru Valley to show peak metamorphic conditions from 33 to 28 Ma were 0.9-1.05 GPa and 620-650 °C with a maximum burial depth of up to 40 km. Finch et al. (2014) also reported a higher P-T range of 550-650 °C and 0.5-0.75 GPa for the biotite to the kyanite zones in SE Zaskar.

Taken together, previous studies show that Suru Valley rocks underwent Barrovian-type metamorphism at ~0.5-1.0 GPa and ~550-650 °C. However, the results of this study show that at peak conditions, Suru Valley rocks were buried more deeply to ~1.10-1.23 GPa at ~550-625 °C. Garnets lack zoning in this study, so this range of P-T conditions does not include the earliest, prograde phase of metamorphism. Figure 14 summarizes the pressure-temperature-time path for Greater Himalayan rocks in Zaskar combining my results with data from Vance and Harris (1999). Additionally, there is a general trend showing a decrease in pressure from the garnet zone (ZH-31 and -34) to the kyanite zone (ZH-39 and -43) in the Suru Dome region. This could have resulted from doming at the later, lower-pressure M<sub>2</sub> event that was associated with anatexis and leucogranite generation in the core of the GHS (Searle et al., 1992; Walker et al., 2001).

## **5.2. Timing of Metamorphism in the Zaskar Himalaya**

There are few U-Pb analyses of metapelites in the Zaskar region. Walker et al. (1999) documented U-Pb ages for monazite of c. 32-28 Ma from schists (their samples WAK 3, WAK 6, and WAK 9) from the SE area of Zaskar, that they interpret to record

M<sub>1</sub> Barrovian-type metamorphism. These data are consistent with c. 34-26 Ma Sm-Nd garnet ages from metapelites associated with the M<sub>1</sub> event in the kyanite zone from Suru Valley in western Zaskar (samples Z93/20 and Z93/24 of Vance and Harris, 1999). These data were confirmed by the  $27.3 \pm 1.2$  Ma U-Pb zircon ages from a garnet schist from the area between Rangdum and Shafat in the Suru Valley (sample Z-40 of Horton and Leech, 2013). Finch et al. (2014) interpreted this range of ages from c. 35 Ma to 17 Ma as a continuum of metamorphism rather than distinct metamorphic events along the P-T path for these rocks. Inger (1998) gives Rb-Sr muscovite ages of c. 26 Ma for micaceous calc-mylonites from Jildo near the ZSZ that they interpret as the age of deformation in the ZSZ (their Z93/31 and Z93/34). This study yields U-Pb zircon ages of  $21.6 \pm 2.7$  Ma and  $17.2 \pm 5.3$  Ma for the area between the ZSZ and the Suru Dome (Fig. 15). I interpret this c. 22 Ma for a sample (ZH-36) taken from mid-Suru Valley to represent an early stage of retrograde metamorphism (see section 5.3 and Table 6); this age may indicate early movement on the ZSZ due to the proximity to the ZSZ as suggested by Hodges et al (1996), Searle et al (1997) for the other segments of the STDS.

There are also U-Pb dates for both granites and schists from the Suru Dome. The Suru Dome is comprised primarily of Miocene granites that are closely-related to the metamorphic history in this region. Noble and Searle (1995) document U-Pb monazite ages for leucogranite from Shafat of 20.8-19.5 Ma and interpret these ages as the timing of crustal melting in the Suru Valley (their sample ZS-14). Inger (1998) gives Rb-Sr ages for muscovite and biotite from the kyanite-staurolite zone in the Suru Dome of c. 20 and c.13 Ma, respectively (sample Z93/20); that study presents another Rb-Sr age for biotite of c. 16 Ma from their sillimanite zone in the Suru Dome (sample Z93/25). Horton and Leech (2013) give ages of 47 to 25 Ma for granites from the Suru Dome and relate these data to their c. 20 Ma age of metamorphism (their sample Z-45). This study presents a U-Pb zircon age of  $19.9 \pm 0.9$  Ma for the Suru Dome from a kyanite-sillimanite schist (ZH-41); the appearance of late fibrolitic sillimanite means that this age indicates the first

stage of retrograde metamorphism (Table 6). I also interpret this  $19.9 \pm 0.9$  Ma age as the minimum age for the onset of the main extensional movement which is a top-to-the-NE normal shearing. This result is slightly younger than the U-Pb zircon age of  $21.6 \pm 2.7$  Ma from mid-Suru Valley (ZH-36) and confirms that the doming event (i.e., Suru Dome) represents a late stage in the thermal history of the Zaskar region (e.g., Searle et al., 1992; Kumar, 1995; Walker et al., 2001).

The westernmost area of Zaskar near Sankoo has more limited age data; Inger (1998) report Rb-Sr ages for muscovite from three schist samples from Sankoo ranging from 30-22 Ma (their samples Z93/1, Z93/3, and Z93/5). This study does not report geochronological data from samples collected from this westernmost part of this area.

Although my U-Pb zircon ages are similar to previously-published ages (see Fig. 14), existing data are insufficient to correlate metamorphic to deformational events for the Zaskar region. However, the transition between the  $M_1$  and  $M_2$  metamorphic events, distinguished by the retrograde minerals, microstructures, and shear sense indicators, could have taken place at c. 20 Ma as summarized in Table 6 that includes the results of all previous studies.

### **5.3. Tectonometamorphic Evolution of the Zaskar Himalaya**

This section contains a combination of petrography and microstructural analysis, thermobarometry and metamorphic modeling, and geo/thermochronological data for the Zaskar region (and more broadly for the GHS) as summarized in Table 6. With the combination of three vital components – time, deformation, and metamorphism – I have generated a the tectonometamorphic model for the Zaskar the region that concatenates results of this and all previous studies.

*Pre-55 Ma:*

The metamorphic rocks of the GHS in Zaskar are considered the high-grade metamorphic equivalents of the unmetamorphosed or weakly-metamorphosed THS, representing different crustal levels in the Indian crust (Walker, 2001).

*~55-50 Ma:*

The initial India-Asia continental collision took place c. 55-50 Ma, comprising the onset of the Himalayan orogeny (Searle et al, 1987; Gaetani and Garzanti, 1991; Klootwijk et al., 1992; Garzanti et al., 1996; Rowley, 1996; Searle et al, 1997; De Celles et al., 2002; 2004; Guillot et al., 2003; Leech et al., 2005).

*~50-33 Ma:*

This is a period of continued India-Asia convergence comprised of Himalayan shortening and Asian contraction. The proto-GHS underwent burial and heating to reach peak metamorphic conditions beneath the Zaskar paleo-thrust fault (Walker, 2001).

*~33-25 Ma:*

The Suru Valley rocks underwent burial and Barrovian-type metamorphism that is seen as a succession of related index minerals, that reached a maximum of kyanite grade. Crustal thickening was achieved as a result of isoclinal folding seen as folding at the outcrop-scale, and as inclusion trails in garnet (see Fig. 5). There is limited geochronological data from garnet cores and rims to distinguish prograde metamorphism, but Vance and Harris (1999) dated garnets from the Suru Valley at 33-28 Ma by Sm-Nd that grew during the initial burial of the GHS. Because garnet cores and rims preserve the metamorphic history of the area, the c. 28 Ma of Vance and Harris (1999) likely records the end of prograde Barrovian-type metamorphism. I use the data from Vance and Harris

(1999) in conjunction with my U-Pb zircon ages to constrain tectonometamorphic events at this stage.

U-Pb zircon ages from samples in the garnet zone of the Suru Valley gave zircon rim ages of  $21.6 \pm 2.7$  and  $17.2 \pm 5.3$  Ma (Fig. 15). These ages are the same within error; I interpret the c. 22 Ma age to record prograde Barrovian-type-metamorphism. Kyanite zone samples that include fibrolitic sillimanite from the Suru Dome gave an age of  $19.9 \pm 0.9$  Ma. Therefore this study suggests that the prograde event lasted until at least c. 22 Ma and then the retrograde event began by c. 20 Ma. Thus it is possible to distinguish these two metamorphic events ( $M_1$  and  $M_2$ ) with these data.

*~25-0 Ma:*

Following the  $M_1$  event and SW-directed thrusting on the ZSZ, deformation in the GHS in the footwall of the ZSZ changed to NE-directed extension. This change was accompanied by anatexis in the GHS, and the exhumation of the GHS from beneath the THS along the ZSZ. Numerous models have been developed to explain tectonometamorphic events during this period including the conventional thrust belt model (Boyer and Elliott, 1982), southward-verging thrust systems (Srivastava and Mitra, 1994), orogenic-scale wedging back-thrusts (Yin, 2006; Webb et al., 2007), and the mid-crustal channel flow model (Grujic et al., 1996; Beaumont et al., 2001). These models explain exhumation of the GHS by syn-orogenic extension along the STDS/ZSZ. The channel flow model is in broad agreement with geological and geophysical evidence (Beaumont et al., 2004) and presents an exciting and relatively new conceptual framework for understanding the geodynamic evolution of crystalline cores of orogenic belts, and a source for continental tectonics studies (Godin et al., 2006). In the channel flow model, the channel material is extruded between the coeval the MCT and the STDS. The GHS acted as a ductile, pervasively-deformed body, instead of a rigid slab (Dèzes, 1999) because partially molten Indian crust was extruded as a result of a lateral pressure

gradient beneath the high Tibetan plateau (Grujic et al., 1996). I do not explore these controversial models beyond this introduction because it is beyond the scope of my study.

U-Pb closure temperature for monazite and zircon shows that the several segments of the STDS (including the age of the ZSZ) cooled at c. 25-20 (this study; Guillot et al., 1994; Harrison et al., 1995; Hodges et al., 1996, Coleman, 1996; Dèzes et al., 1999) and that is interpreted as a minimum age for the onset of normal motion along the STDS.

The last stage of the tectonometamorphic model is constrained by the closure temperatures of muscovite (~400 °C) and biotite (~300 °C) (Spear, 1993; McDougall and Harrison, 1999). The late-stage doming event that created the Suru Dome caused large-scale doming of the  $M_1$  isograds in the GHS as proposed in Walker (2001). Rb-Sr dating of muscovite and biotite from the Zaskar region give ages c. 26-21 Ma and c. 13-11 Ma, respectively (Honegger et al., 1982). They compared these results with tectonostratigraphic-equivalent units from Bhutan, Nepal, and Kulu-Lahul and showed that the late cooling history is similar along the Himalaya over a distance of ~2000 km. Inger (1998) dated metapelites from along the Suru Valley, using Rb-Sr geochronology on muscovite and biotite that indicates c. 34-18 Ma and c. 16-12 Ma respectively. A K-Ar biotite age of c. 20 Ma from Sankoo in the western part of Suru Valley (Fig. 2), and a granite from Parkatchic in the Suru Dome gives  $^{40}\text{Ar}/^{39}\text{Ar}$  muscovite and biotite cooling ages of c. 15 Ma and c. 13 Ma, respectively (Searle et al., 1992). This range of cooling ages from Searle et al (1992) and Inger (1998) shows that cooling in the eastern section of the Suru Valley started later than in the western part. The cooling history is constrained by Rb-Sr, K-Ar, and  $^{40}\text{Ar}/^{39}\text{Ar}$  thermochronology in the range of c. 24-14 Ma for biotite, and c. 23-20 Ma for muscovite in the Zaskar region (Spring et al., 1993; Sorkhabi et al., 1997; Walker et al., 1999; Dèzes et al., 1999). These data are in agreement with U-Pb ages of c. 20 Ma for the Suru Dome from this study, recording the

broad doming event that occurred in this late stage of metamorphism (Table 6). Because of this doming and crustal anatexis, the Suru Dome re-equilibrated after the peak  $M_1$  metamorphism (Searle et al., 1992, Walker et al., 1999), and uplift is continuing (Dèzes, 1999; Walker et al., 1999; Walker et al., 2001).

## 5. CONCLUSIONS

1. Field observations, petrographic analysis, and regional mapping of metamorphic isograds in this study indicate a complete prograde Barrovian-type metamorphism from the chlorite-biotite zone to the kyanite zone. Post-  $M_1$  metamorphism shearing along the ZSZ and MCT narrowed these metamorphic zones to ~15 km in western Zanskar (this study) and to only ~500 m in central and eastern Zanskar (Inger, 1998; Dèzes, 1999).

2. Micro-scale shear sense indicators in Zanskar rocks such as C-C' fabrics, rotated garnet porphyroblasts, and mineral fish reveals that a top-to-the-SW thrusting was overprinted by a top-to-the-NE normal shearing. I observed both coplanar- and co-directional-sense evidence for thrusting and normal shearing.

3. The temperature slightly increases from the garnet zone to the kyanite zone based on my pseudosection modeling results. Different types of dynamic recrystallization of quartz grains suggest the temperatures of deformation increased from the ZSZ southward. Peak temperatures calculated using Fe-Mg exchange thermometry for garnet and biotite (Ferry and Spear, 1978; Hodges and Spear, 1982) are ~620 °C in the garnet zone and ~700 °C in the kyanite zone in the Suru Dome. The ~700 °C temperature calculated for the Suru Dome suggests the  $M_2$  event was associated with crustal anatexis as proposed by Searle et al (1999) and Walker et al (2001).

4. Pressure decreases from the ZSZ to the Suru Dome due to the late doming event associated with crustal anatexis. Pressure for the  $M_1$  event of 0.95-1.05 GPa decreases to 0.87-0.97 GPa for the  $M_2$  event recorded in the Suru Dome (Walker et al., 2001). The difference between these values (at a maximum, ~0.18 GPa) belonging to two different metamorphic stages is in agreement with the data from this study in which I show the pressure decreases from 1.18-1.23 GPa for  $M_1$  to 1.10 GPa for  $M_2$  for the Suru Dome rocks.

5. The summary P-T path estimated for samples in this study does not include any burial data due to a lack of strong zoning in garnet porphyroblasts. P-T conditions were constrained to a range of ~1.10-1.23 GPa at ~550-625 °C for four samples in this study. Prograde heating and post-peak near isobaric cooling reflects typical Himalayan collisional tectonics and showing a common clockwise P-T path for the Zaskar region.

6. Understanding the evolution of the Himalayan orogen requires understanding the history and mechanisms of exhumation and the timing and conditions of metamorphism. The calculated peak pressures suggest that following India-Asia collision, during burial of GHS rocks, prograde Barrovian-type  $M_1$  metamorphism reached a maximum kyanite grade at ~1.25 GPa in the Suru Valley.

7. Sm-Nd dating on garnet indicates that garnet grew at ~33-28 Ma (Vance and Harris, 1999) recording the  $M_1$  event. However, results from this study suggests that garnet growth stopped ~22 Ma. Crustal thickening was followed by rapid exhumation of the GHS beneath the ZSZ at c. 22 Ma (Table 6). The doming event creating the Suru Dome occurred before  $19.9 \pm 0.9$  Ma as indicated by U-Pb geochronology of metamorphic zircons from the Suru Dome.

8. Assuming a geothermal gradient of ~0.03 GPa per km, a greater amount of overburden (>30 km) can also explain the greater pressures reached by samples in the Suru Valley.

9. Prograde Barrovian-type regional metamorphism of the GHS took place ~33-25 Ma at 550-650 °C and 0.8-1.2 GPa following the India-Asia collision that began at c. 55 Ma. During this period, crustal thickening occurred with SW-directed thrusting on the ZSZ. After crustal thickening, a second, retrograde metamorphic event began when motion on the ZSZ switched from thrusting to normal shearing no later than c. 22 Ma based on U-Pb zircon data in this study. This orogen-wide tectonic change caused rapid exhumation of the GHS from beneath the THS with decreased pressure and a temperature

increase to  $\sim 700$  °C. This exhumation process caused by decompression melting and/or dehydration of hydrous minerals in the middle Indian crust (the GHS) correlates to coeval motion on the ZSZ and the MCT. The Suru Dome rocks re-equilibrated as a result of the doming event and crustal anatexis at c. 20 Ma. As a consequence of Himalayan uplift since then, one of the youngest, highest, longest, and the most tectonically active mountain range on Earth was created.

**REFERENCES**

- Auzanneau, E., Schmidt, M.W., Vielzeuf, D. and Connolly, J.A.D., 2010, Titanium in phengite: a geobarometer for high temperature eclogites: *Contributions to Mineralogy and Petrology*, v. 159, p. 1–24.
- Barth, A.P., and Wooden, J.L., 2010, Coupled elemental and isotopic analyses of polygenetic zircons from granitic rocks by ion microprobe, with implications for melt evolution and the source of granitic magmas: *Chemical Geology*, v. 277, p. 149–159.
- Black, L.P., Kamo, S.L., Allen, C.M., Davis, D.W., Aleinikoff, J.N., Valley, J.W., Mundil, R., Campbell, I.H., Korsch, R.J., Williams, I.S., and Foudoulis, C., 2004, Improved  $^{206}\text{Pb}/^{238}\text{U}$  microprobe geochronology by the monitoring of a trace-element-related matrix effect; SHRIMP, ID-TIMS, ELA-ICP-MS and oxygen isotope documentation for a series of zircon standards: *Chemical Geology*, v. 205, p. 115–140, doi: <http://dx.doi.org/10.1016/j.chemgeo.2004.01.003>.
- Burchfiel, B.C., Chen, Z.L., Hodges, K.V., Liu, Y.P., Royden, L.H., Deng, C.R., and Xu, J.N., 1992, The South Tibetan detachment system, Himalayan Orogen: Extension contemporaneous with and parallel to shortening in a collisional mountain belt: *Geological Society of America Special Paper 269*, 41 p.
- Coggon, R., and Holland, T. J. B., 2002, Mixing properties of phengitic micas and revised garnet phengite thermobarometers: *Journal of Metamorphic Geology*, v. 20, p. 683–696.
- Coleman, M.E., 1998, U-Pb constraints on Oligocene-Miocene deformation and anatexis within the Central Himalaya, Marsyandi valley, Nepal: *American Journal of Science*, v. 298, p. 553–571.

- DeCelles, P.G., Robinson, D.M., Zandt, G., 2002, Implications of shortening in the Himalayan fold–thrust belt for uplift of the Tibetan plateau: *Tectonics*, v. 21, doi:10.1029/2001TC001322.
- DeCelles, P.G., Gehrels, G.E., Najman, Y., Martin, A.J., Carter, A., Garzanti, E., 2004, Detrital geochronology and geochemistry of cretaceous–early Miocene strata of Nepal: implications for timing and diachroneity of initial Himalayan orogenesis: *Earth and Planetary Science Letters*, v. 227, p. 313–330.
- Dèzes, P., 1999, Tectonic and metamorphic evolution of the Central Himalayan Domain in Southeast Zaskar (Kashmir, India) [Ph.D. thesis]: University of Lausanne, 149 p.
- Dèzes, P. J., Vannay, J.-C., Steck, A., Bussy, F., and Cosca, M., 1999, Synorogenic extension: Quantitative constraints on the age and displacement 1185 of the Zaskar shear zone (northwest Himalaya): *Geological Society of America Bulletin*, v. 111, p. 364–374.
- Ferry, J.M. and Spear, F.S., 1978, Experimental calibration of the partitioning of Fe and Mg between biotite and garnet: *Contributions to Mineralogy and Petrology*, v. 66, p. 113–117.
- Frank, W., Thöni, M., Purtscheller, F., 1977, Geology and petrography of Kulu-South Lahul area: *Colloques internationaux CNRS (Paris)*, v. 268, p. 147–160.
- Fuhrman, M.L. and Lindsley, D.H., 1988, Ternary-feldspar modeling and thermometry: *American Mineralogist*, v. 73, p. 201–215.
- Gaetani, M., Garzanti, E., 1991, Multicyclic history of the northern India continental margin (northwestern Himalaya): *American Association of Petroleum Geologists Bulletin*, v. 75, p. 1427–1446.

- Gaidies, F., Abart, R., De Capitani, C., Schuster, R., Connolly, J.A.D., Reusser E., 2006, Characterization of polymetamorphism in the Austroalpine basement east of the Tauern Window using garnet isopleth thermobarometry: *Journal of Metamorphic Geology*, v. 24, p. 451–475
- Garzanti, E., Critelli, S., Ingersoll, R.V., 1996, Paleogeographic and paleotectonic evolution of the Himalayan range as reflected by detrital modes of tertiary sandstones and modern sands (Indus transect, India and Pakistan): *Geological Society of America Bulletin*, v. 108, p. 631– 642.
- Gilbert, E., 1986, *Évolution structurale d'une chaîne de collision: Structures et déformation dans le nord de la plaque indienne en Himalaya du Ladakh (cristallin de haut Himalaya et séries téthysiennes)*. [Ph.D. thesis]: Université de Poitiers. 225 p.
- Godin, L., Parrish, R. R., Brown, R. L. & Hodges, K. V., 2001, Crustal thickening leading to exhumation of the Himalayan metamorphic core of central Nepal: insight from U-Pb geochronology and  $^{40}\text{Ar}/^{39}\text{Ar}$  thermochronology: *Tectonics*, v. 20, p. 729–747.
- Godin, L., Grujic, D., Law, R.D., and Searle, M.P., 2006, Channel flow, ductile extrusion and exhumation in continental collision zones: An introduction, in Law, R.D., Searle, M.P., and Godin, L., eds., *Channel flow, ductile extraction and exhumation in continental collision zones*: London, Geological Society Special Publication, v. 268, p. 1–23.
- Guillot, S., Garzanti, S., Baratoux, E., Marquer, D., Mahe' o, D., de Sigoyer, J., 2003, Reconstructing the total shortening history of the NW Himalaya: *Geochemistry Geophysics Geosystems*, v. 4, doi:10.1029/2002GC000484.

- Harris, N.B.W., Caddick, M., Kosler, J., Goswami, S., Vance, D., and Tindle, A.G., 2004, The pressure-temperature-time path of migmatites from the Sikkim Himalaya: *Journal of Metamorphic Geology*, v. 22, p. 249–264.
- Heaman, L., and Parrish, R., 1991, U-Pb geochronology of accessory minerals. In L. Heaman and J.N. Ludden, Eds., *Short course handbook on applications of radiogenic isotope systems to problems in geology: Mineralogical Association of Canada*, v. 19, p. 59–102.
- Herren, E., 1987, Zaskar shear zone: Northeast-southwest extension within the Higher Himalayas (Ladakh, India): *Geology*, v. 15, p. 409–413.
- Hodges, K.V., and Spear, F.S., 1982, Geothermometry, geobarometry, and the  $\text{Al}_2\text{SiO}_5$  triple point at Mt. Moosilauke, New Hampshire: *American Mineralogist*, v. 67, p. 1118–1134.
- Holland, T. J. B., and Powell, R., 1998, An internally consistent thermodynamic dataset for phases of petrological interest: *Journal of Metamorphic Geology*, v. 16, p. 309–343.
- Honegger, K., Dietrich, V., Frank, W., Gansser, A., Thöni, M., Trommsdorf, V., 1982, Magmatism and metamorphism in the Ladakh Himalaya (the Indus-Tsangpo suture zone): *Earth and Planetary Science Letters* v. 60, p. 253–292.
- Honegger, K., 1983, *Strukturen und Metamorphose im Zaskar Kristallin* [Ph.D. thesis]: EHT Zurich, 117 p.
- Horton, F., and Leech, M. L., 2013, Age and origin of granites in the Karakoram shear zone and Greater Himalaya Sequence, NW India: *Lithosphere*, v. 5, p. 300–320.

- Inger, S., 1998, Timing of an extensional detachment during convergent orogeny: New Rb-Sr geochronological data from the Zaskar Shear Zone, northwestern Himalaya: *Geology*, v. 26, p. 223–226.
- Ireland, T.R., and Williams, I.S., 2003, Considerations in Zircon Geochronology by SIMS: *Reviews in Mineralogy and Geochemistry*, v. 53, p. 215–241.
- Klootwijk, C. T., Gee, J.S., Peirce J.W., Smith, G.M., McFadden, P.L., 1992, An early India–Asia contact: paleomagnetic constraints from Ninetyeast Ridge, ODP Leg 121: *Geology*, v. 20, p. 395–398.
- Kumar, A., Lal, N., Jain, A. K., Sorkhabi, R. B., 1995, Late Cenozoic–Quaternary thermo-tectonic history of Higher Himalayan crystalline (HHC) in Kishtwar-Padar-Zaskar region, NW Himalaya: Evidence from fission track ages: *Geological Society of India Journal*, v. 45, p. 375–391.
- Kundig, R., 1989, Domal structures and high-grade metamorphism in the Higher Himalayan Crystalline, Zaskar region, northwest Himalaya, India: *Journal of Metamorphic Geology*, v. 7, p. 43–55.
- Leech, M.L., Singh, S., Jain, A.K., Klemperer, S.L., Manickavasagam, R.M., 2005, The onset of India-Asia continental collision: Early, steep subduction required by the timing of UHP metamorphism in the western Himalaya: *Earth and Planetary Science Letters*, v. 234, p. 83–97.
- Ludwig, K.R., 2009, Squid 2, A user manual, Berkeley Geochronology Center Special Publication No. 5.
- Ludwig, K.R., 2012, Isoplot (3.75), a geochronological toolkit for Excel, Berkeley Geochronology Center Special Publication No. 5, p. 75.

- McDougall, I., and T.M. Harrison, 1999, *Geochronology and Thermo-chronology by the  $^{40}\text{Ar}/^{39}\text{Ar}$  Method*, 2nd Edition. Oxford University Press, New York, NY.
- Mehta, P.K., 1977, Rb/Sr geochronology of the Kulu-Mandi belts: its implication for the Himalayan Tectogenesis: *Geologische Rundschau*, v. 66, p. 156–175.
- Mukherjee, S. and Koyi, H.A., 2010, Higher Himalayan shear zone, Zaskar Indian Himalaya—microstructural studies and extrusion mechanism by a combination of simple shear and channel flow: *International Journal of Earth Sciences*, v. 99, p. 1083–1110.
- Noble, S. R., and Searle, M. P., 1995, Age of crustal melting and leucogranite formation from U-Pb zircon and monazite dating in the western Himalaya, Zaskar, India: *Geology*, v. 23, p. 1135–1138.
- Noble, S. R., Searle, M. P., and Walker, C. B., 2001, Age and tectonic significance of Permian granites in Western Zaskar, High Himalaya: *The Journal of Geology*, v. 109, p. 127–135.
- Passchier, C. W. and Trouw, R. A. J., 2005. *Microtectonics*. Springer-Verlag, Berlin, 366 p.
- Powell, R., and Holland, T.J.B, 1988, An internally consistent thermodynamic dataset with uncertainties and correlations: 3. Applications to geobarometry, worked examples and a computer program: *Journal of Metamorphic Geology*, v. 6, p. 173–204.
- Rowley, D.B., 1996, Age of initiation of collision between India and Asia: A review of stratigraphic data: *Earth Planetary Science Letters*, v. 145, p. 1–13.

- Searle, M.P., and Fryer, B.J., 1986, Garnet, tourmaline and muscovite-bearing leucogranites, gneisses and migmatites of the Higher Himalayas from ZaskarKulu, Lahoul and Kashmir, in Coward, M.P., and Ries, A.C., eds., Collision Tectonics: Geological Society of London Special Publication No. 19, p. 185–201.
- Searle, M.P., Windley, B.F., Coward, M.P., 1987, The closing of Tethys and the tectonics of the Himalaya: Geological Society of America Bulletin, v. 98, p. 678–701.
- Searle, M. P., and Rex, A. J., 1989, Thermal model for the Zaskar Himalaya: Journal of Metamorphic Geology, v. 7, p. 127–134.
- Searle, P. M., Waters, J. D., Rex, C. D., et al., 1992, Pressure, temperature and time constraints on Himalayan metamorphism from eastern Kashmir and western Zaskar: Journal of the Geological Society, London, v. 149, p. 753–773.
- Searle, M.P., Parrish, R.R., Hodges, K.V., Hurford, A., Ayres, M.W. and Whitehouse, M.J., 1997, Shisha Pangma leucogranite, South Tibetan Himalaya: field relations, geochemistry, age, origin and emplacement: Journal of Geology, v. 105, p. 295–317.
- Searle, M. P., Waters, D. J., Dransfield, M. W., Stephenson, B. J., Walker, C. B., Walker, J.D., and Rex, D. C., 1999, Thermal and mechanical models for the structural and metamorphic evolution of the Zaskar High Himalaya, *in* Mac Niocail, C., Ryan, P.D., eds., Continental Tectonics: Geological Society [London] Special Publication 164, 1422 p. 139–156.
- Simpson, C. and Wintch, R.P., 1989, Evidence for deformation-induced K-feldspar replacement by myrmekite: Journal of Metamorphic Geology, v. 7, p. 261–275.

- Sorkhabi, R. B., Jain, A. K., Itaya, T., Fukui, S., Lal, N. and Kumar, A., 1997, Cooling age record of domal uplift in the core of the Higher Himalayan Crystallines (HHC), southwest Zaskar, India: *Proc. Indian Acad. Sci. (Earth Planet. Sci.)*, v. 106, p. 169–179.
- Spear, F.S., 1993, *Metamorphic Phase Equilibria and Pressure-Temperature-Time Paths*: Mineralogical Society of America, Washington, D. C., 799 p.
- Spring, L., Bussy, F., Vannay, J. C., Houn, S., Cosca, M. A., 1993, Early Permian granitic dykes of alkaline affinity in the Indian High Himalaya of Upper Lahul and SE Zaskar: geochemical characterization and geotectonic implications: *Himalayan Tectonics Geological Society Special Publication*, v. 74, p. 251-264.
- Stacey, J.S., and Kramers, J.D., 1975, Approximation of terrestrial lead isotope evolution by a two-stage model: *Earth and Planetary Science Letters*, v. 26, p. 207–221.
- Stäubli, A., 1989, Polyphase metamorphism and the development of the Main Central Thrust: *Journal of Metamorphic Geology*, v. 7, p. 73–93.
- Stipp, M., Stünitz, H., Heilbronner, R., and Schmid, S. M., 2002, The eastern Tonale fault zone: a ‘natural laboratory’ for crystal plastic deformation of quartz over a temperature range from 250 to 700 °C: *Journal of Structural Geology*, v. 24, p. 1861–1884.
- Stutz, E., and Thöni, M., 1987, The lower Paleozoic Nyimaling Granite in the Indian Himalaya (Ladakh): New Rb/Sr data versus zircon typology: *Geologische Rundschau*, v. 76, p. 307–315.
- Tajcmanova, L., Connolly, J.A.D., and Cesare, B., 2009, A thermodynamic model for titanium and ferric iron solution in biotite: *Journal of Metamorphic Geology*, v. 27, p. 153–165.

- Tera, G., and Wasserburg, T. F., 1972, U-Th-Pb systematics 1437 in three Apollo 14 basalts and the problem of initial Pb in lunar rocks: *Earth and Planetary Science Letters*, v. 14, p. 281–304.
- Vance, D. and Mahar, E., 1998, Pressure-temperature paths from P-T pseudosections and zoned garnets: potential, limitations and examples from the Zaskar Himalayas, NW India: *Contributions to Mineralogy and Petrology*, v. 132, p. 225–245.
- Vance, D. and Harris, N., 1999, Timing of prograde metamorphism in the Zaskar Himalaya: *Geology*, v. 27, 395–398.
- Vannay, J. C. and Hodges, K. V., 1996, Tectonometamorphic evolution of the Himalayan metamorphic core between Annapurna and Dhaulagiri, central Nepal: *Journal of Metamorphic Geology*, v. 14, p. 635–656
- Vernon, R. H., 2004. A practical guide to rock microstructure. Cambridge University Press, 606 p.
- Walker, C. B., Searle, M. P., and Waters, D. J., 2001, An integrated tectonothermal model for the evolution of the High Himalaya in western Zaskar with constraints from thermobarometry and metamorphic modeling: *Tectonics*, v. 20, p. 810–833.
- Walker, J. D., Martin, M. W., Bowring, S. A., Searle, M. P., Waters, D. J., and Hodges, K. V., 1999, Metamorphism, melting, and extension: Age constraints from the High Himalayan Slab of Southeast Zaskar and Northwest Lahaul: *The Journal of Geology*, v. 107, p. 473–495.
- White, R.W., Powell, R., Holland, T. J. B., and Worley, B. A., 2000, The effect of TiO<sub>2</sub> and Fe<sub>2</sub>O<sub>3</sub> on metapelitic assemblages at greenschist and amphibolite facies conditions: mineral equilibria calculations in the system K<sub>2</sub>O-FeO-MgO-Al<sub>2</sub>O<sub>3</sub>-SiO<sub>2</sub>-H<sub>2</sub>O-TiO<sub>2</sub>-Fe<sub>2</sub>O<sub>3</sub>: *Journal of Metamorphic Geology*, v. 18, p. 497–511.

Whitney, D. L. And Evans, B. W., 2010, Abbreviations for names of rock-forming minerals: *American Mineralogist*, v. 95, p. 185–187.

Williams, I.S., 1997, U-Th-Pb geochronology by ion microprobe: not just ages but histories: *Society of Economic Geologists Review*, v. 7, p. 1–35.

## FIGURES

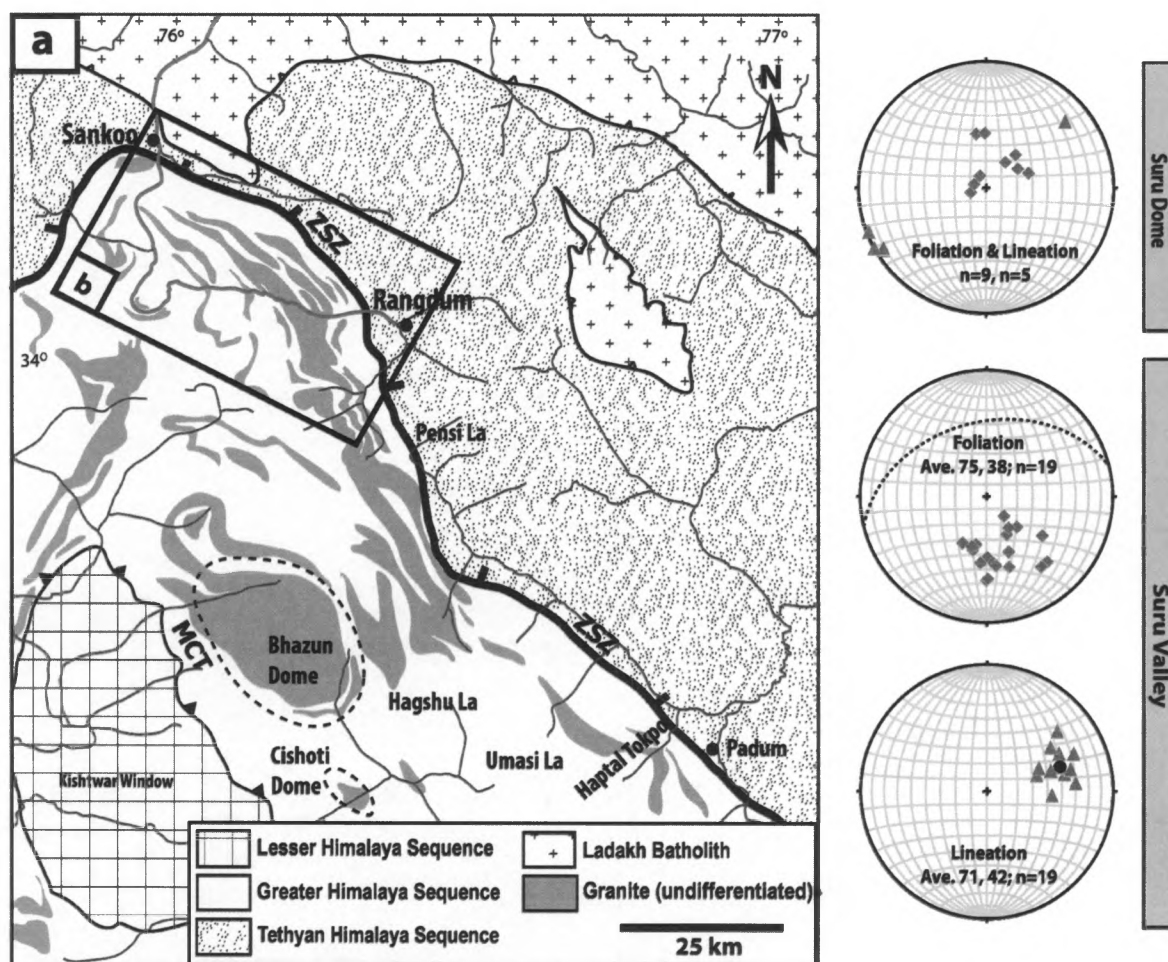


**Figure 1.** (a) Simplified geological map of the Zaskar area (modified from Horton and Leech, 2013) showing (b) the study area in Suru Valley. ZSK: The Zaskar Shear Zone, MCT: The Main Central Thrust. Structural data for the Suru Dome and the Suru Valley are shown as poles to foliation (grey diamonds) and lineations (grey triangles). The mean foliation plane (dashed black great circle) and mean lineation (black circle) are shown for Suru Valley. The domal foliation around Suru Dome overprints Suru Valley structures.

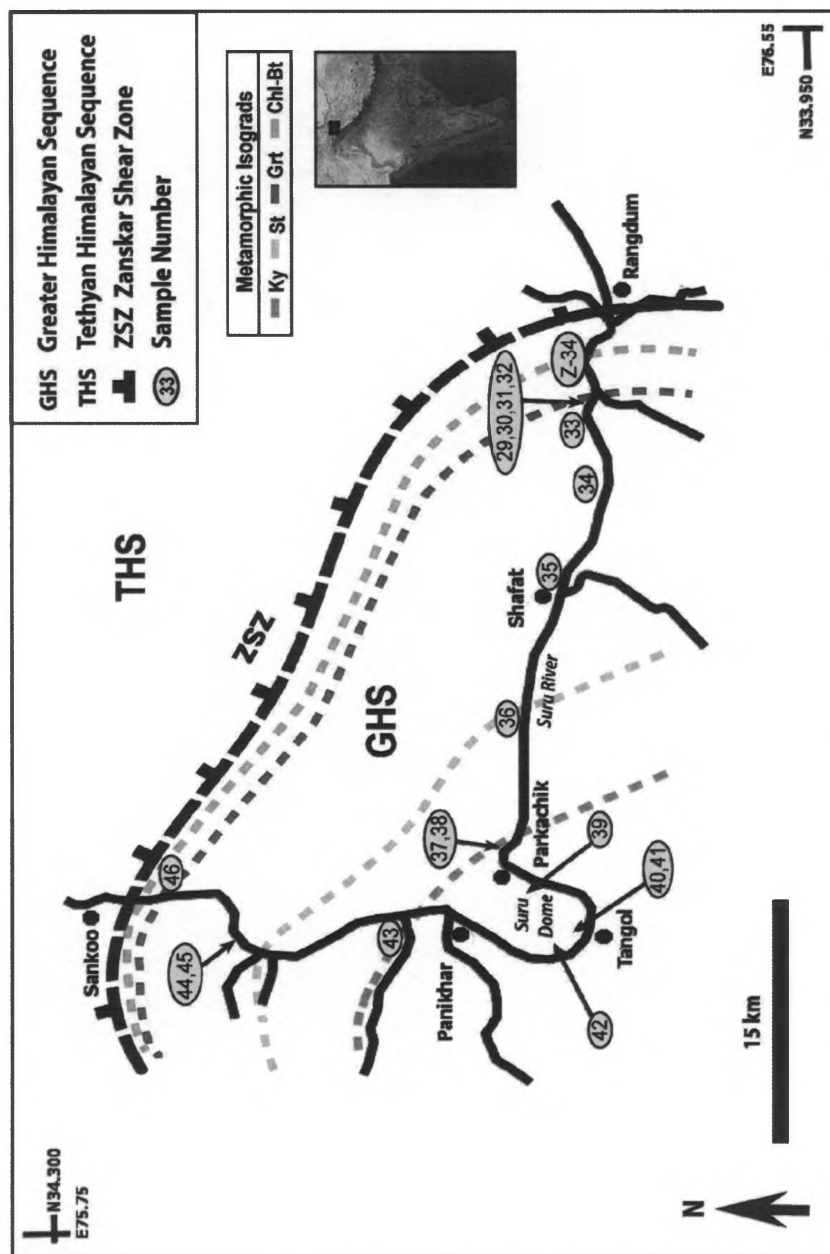


**Figure 2.** Simplified geological map of Suru Valley (modified from Google Earth imagery) in Fig. 1b with all sample locations, showing metamorphic isograds. The location of the ZSZ is adapted from Searle et al. (1992), Vance and Harris (1999), and Noble et al. (2001). Approximate metamorphic isograds as a result of this study are shown from the Chl-Bt zone closest to the ZSZ through the Ky zone at greater structural depths near Suru Dome. The positions of isograds between sample ZH-43 and Sankoo are estimates because samples lacked the appropriate index minerals. Retrograde sillimanite is only found in ZH-41 in the Suru Dome. The “ZH” prefix was dropped from those sample numbers for clarity. Mineral abbreviations are from Whitney and Evans (2010), see also Table 2.

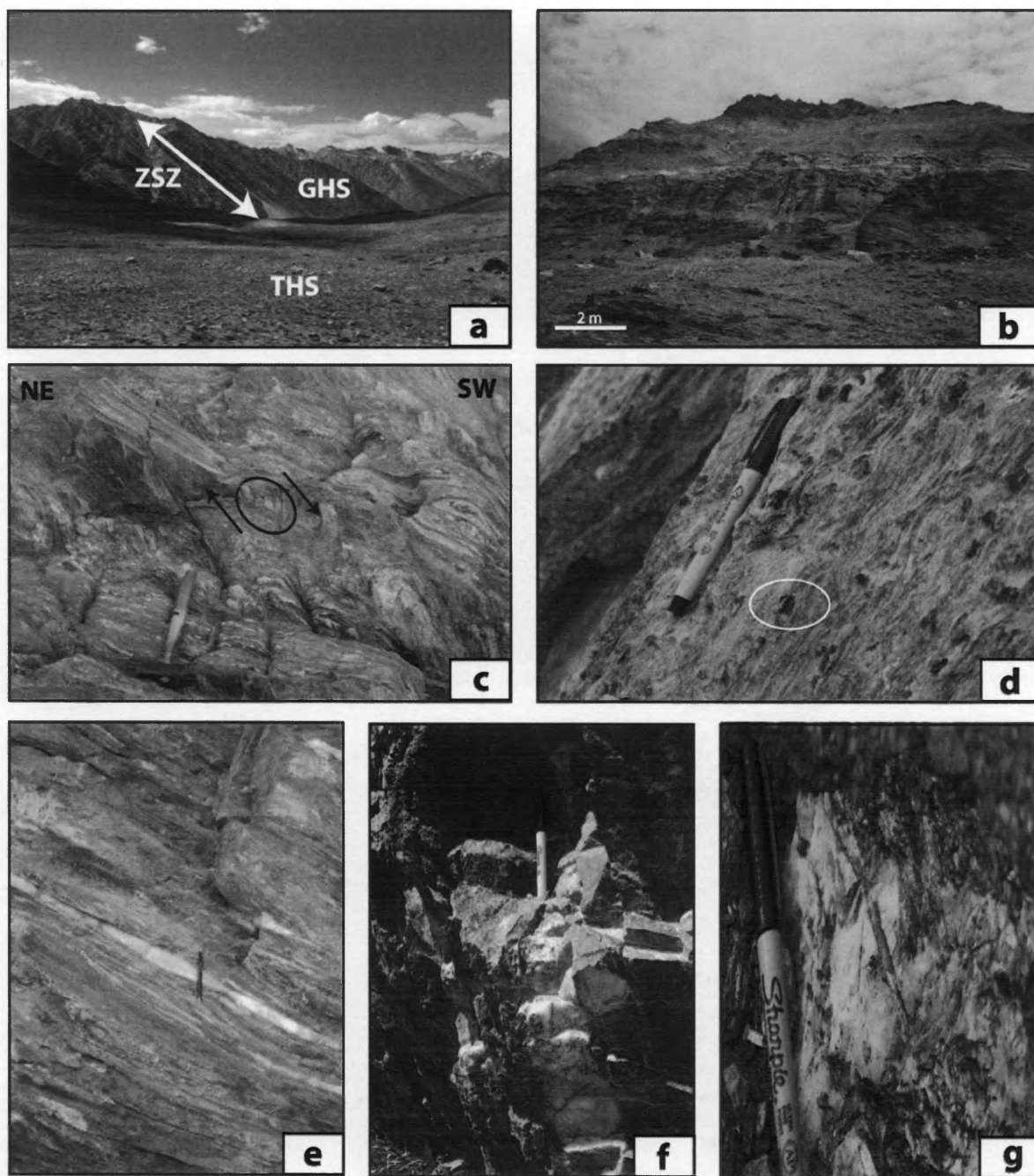


**Figure 3.** Field and outcrop photos of the Zanskar area. (a) Faceted range front of the GHS along the Zanskar Shear Zone separating the GHS from the THS along the Doda River. (b) The Suru Dome with intrusion of leucogranitic dikes (c) Centimeter-scaled asymmetric folds with  $\sigma$ -type mantled quartz porphyroclasts (circled) in schist indicating both a top-to-the-SW thrusting from Shafat. (d) Snowball garnets in schist from the southern part of Suru Valley. (e) No-slip quartz boudinage (symmetric), parallel to stretching lineation. (f) Cross-cutting leucocratic dike in schist. (g) Kyanite from the Suru Dome.

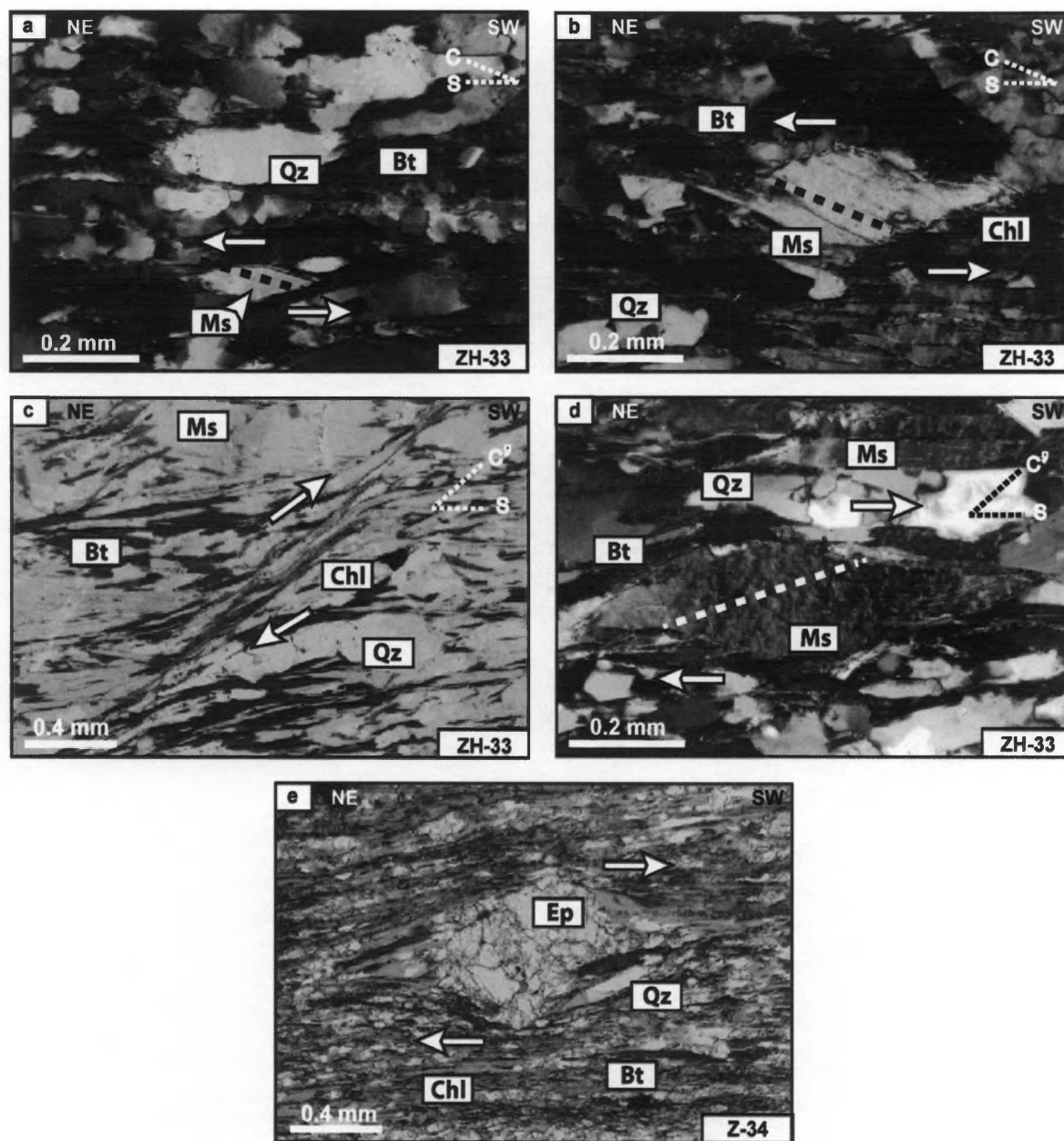


**Figure 4.** Photomicrographs indicating both a top-to-the-SW and a top-to-the-NE shear senses. (a) Top-to-the-NE normal shear is displayed by quartz and parallelogram-shaped muscovite fish. The muscovite cleavage is shown by black dashed line (XPL). (b) Mica fish showing a top-to-the-NE shear sense (XPL). (c) A top-to-the-SW thrusting indicated by the C' plane. Note the retrograde growth of chlorite on C' plane (PPL). (d) Mica fish indicating a top-to-the-SW thrusting. The muscovite cleavage is shown by white dashed line. (e) Pseudomorph of epidote group minerals from the chlorite-biotite zone, showing a top-to-the-SW shear sense (PPL). Mineral abbreviations are from Whitney and Evans (2010), see also Table 2.

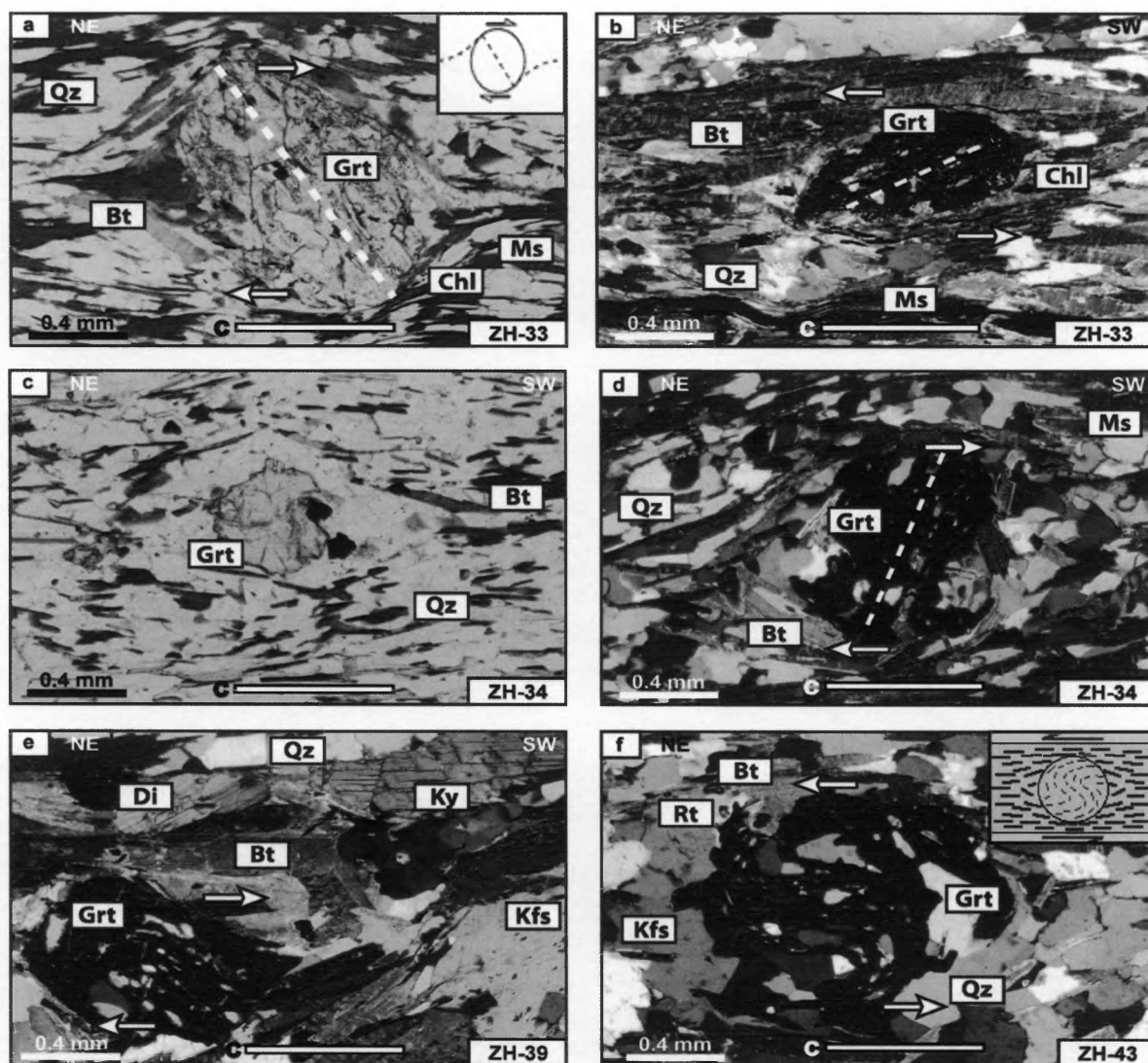


**Figure 5.** Photomicrographs of garnets indicating both a top-to-the-SW and a top-to-the-NE shear senses. The C plane is shown by the white line at the bottom of each photo. Inclusion trails in garnet poikiloblasts are shown by dashed white lines, and shear sense is indicated by the white arrows. (a) Syn-tectonic garnet poikiloblast from the garnet zone with straight inclusion trails containing Qz + Pl + Bt (PPL). The inset box shows geometrical relationship between internal foliation indicated by inclusion trails and external foliation in the matrix, and shear sense. (b and e) Syn-tectonic garnet fish with straight inclusion trails (XPL). (c) Pre-tectonic garnet showing strong foliation deflection and randomly oriented inclusions (PPL). (d) Syn-tectonic garnet with straight inclusion trails (XPL). (f) Syn-tectonic snowball garnet with curved quartz and rutile inclusion trails that are continuous with the matrix (XPL). The inset box shows the continuity between internal and external foliation in garnet, and shear sense. Shear sense criteria indicates a top-to-the-NE rotation of  $\sim 120^\circ$ . Mineral abbreviations are from Whitney and Evans (2010), see Table 2.

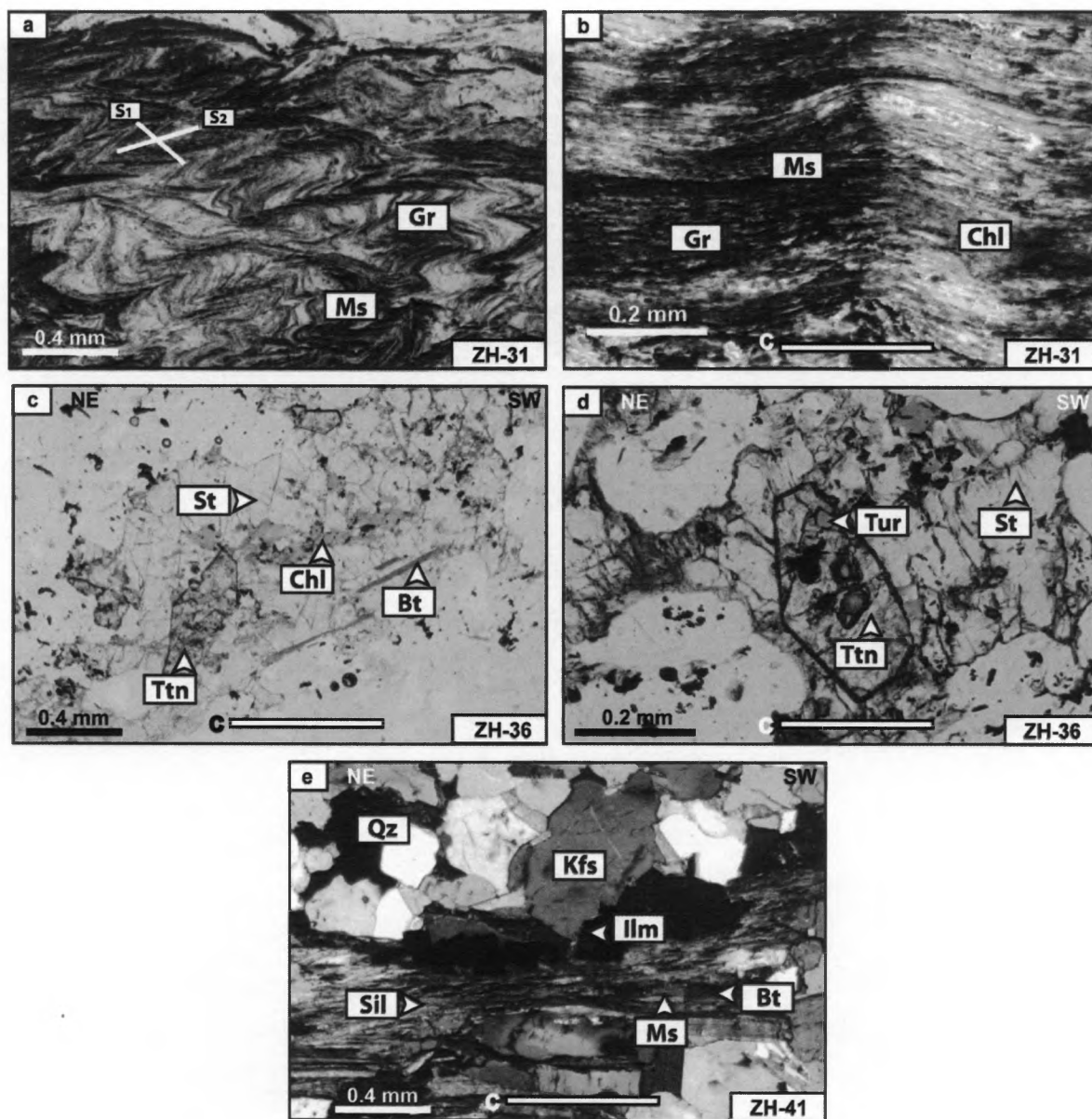


**Figure 6.** Photomicrographs of representative rocks fabrics. (a) Graphite decorated foliation with muscovite from the garnet zone. It also shows an asymmetric crenulation cleavage ( $S_2$ ) overprinting an  $S_1$  cleavage (PPL). (b) Microfolds and kinked aggregate of muscovite, chlorite, and graphite from the garnet zone (XPL). (c) Biotite preserved in titanite preserved in staurolite. Note that orientation of biotite in both titanite and staurolite defines an earlier foliation (PPL). (d) Tourmaline inclusions in titanite, both preserved in staurolite. The yellow color is a remnant of gold-coating (PPL). (e) Fibrolitic sillimanite replacing muscovite is present with ilmenite from the kyanite zone in the Suru Dome. Fibrolite is parallel to the C plane (XPL). Mineral abbreviations are from Whitney and Evans (2010), see Table 2.

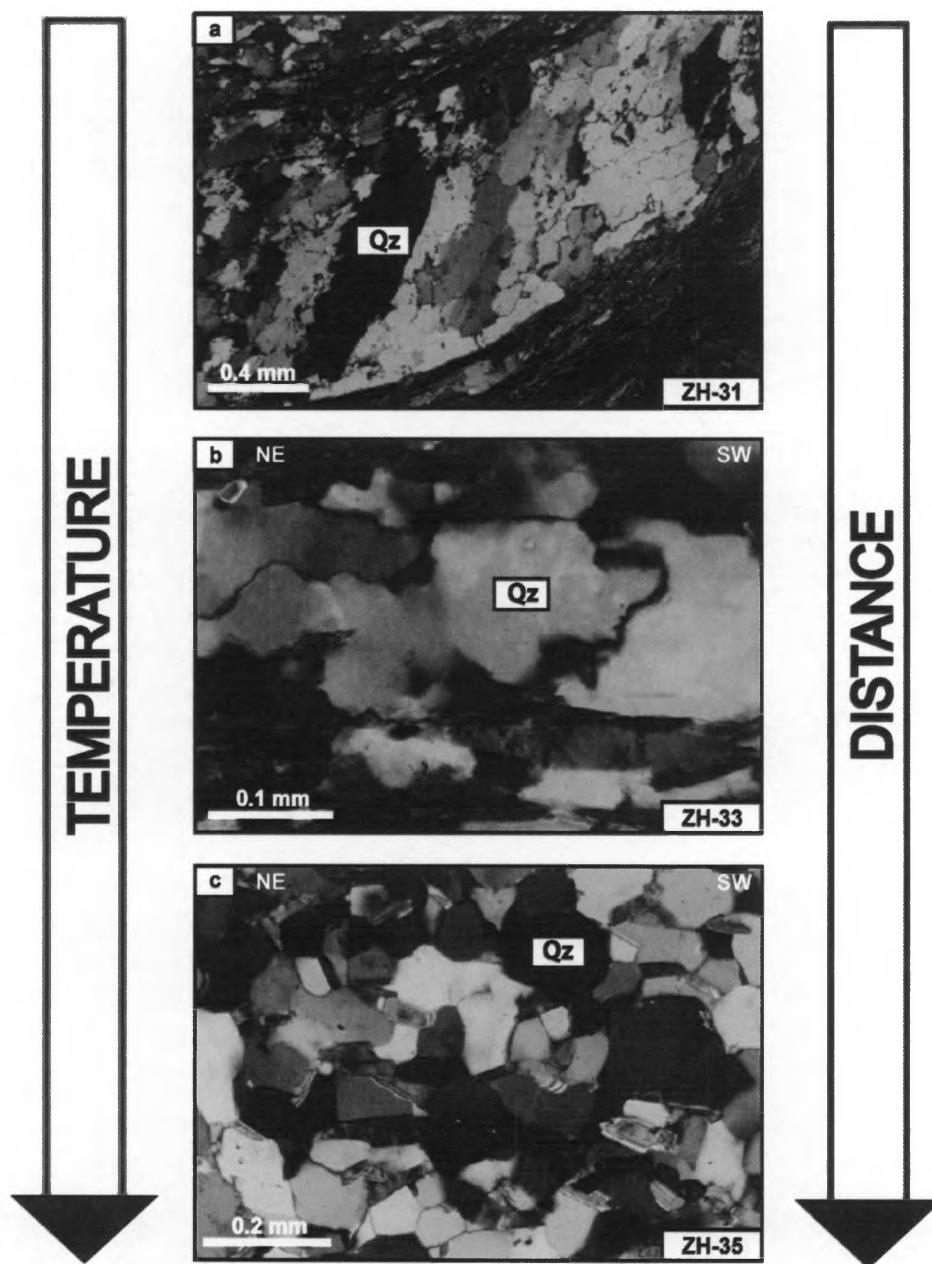


**Figure 7.** Photomicrographs showing a relationship between quartz fabrics with increasing distance from the ZSZ and temperature (a) Subgrain rotation of quartz grains from dynamic recrystallization between graphitic microfolds (~3 km from the ZSZ). (b) Deeply sutured boundaries in quartz quartz showing dynamic recrystallization through grain boundary migration (~5 km from the ZSZ). (c) Euhedral quartz grains exhibiting polygonal grain boundaries (~15-20 km from the ZSZ). There is almost no visible evidence for dynamic recrystallization in this sample near Shafat. All photomicrographs are in XPL. Mineral abbreviations are from Whitney and Evans (2010), see also Table 2.

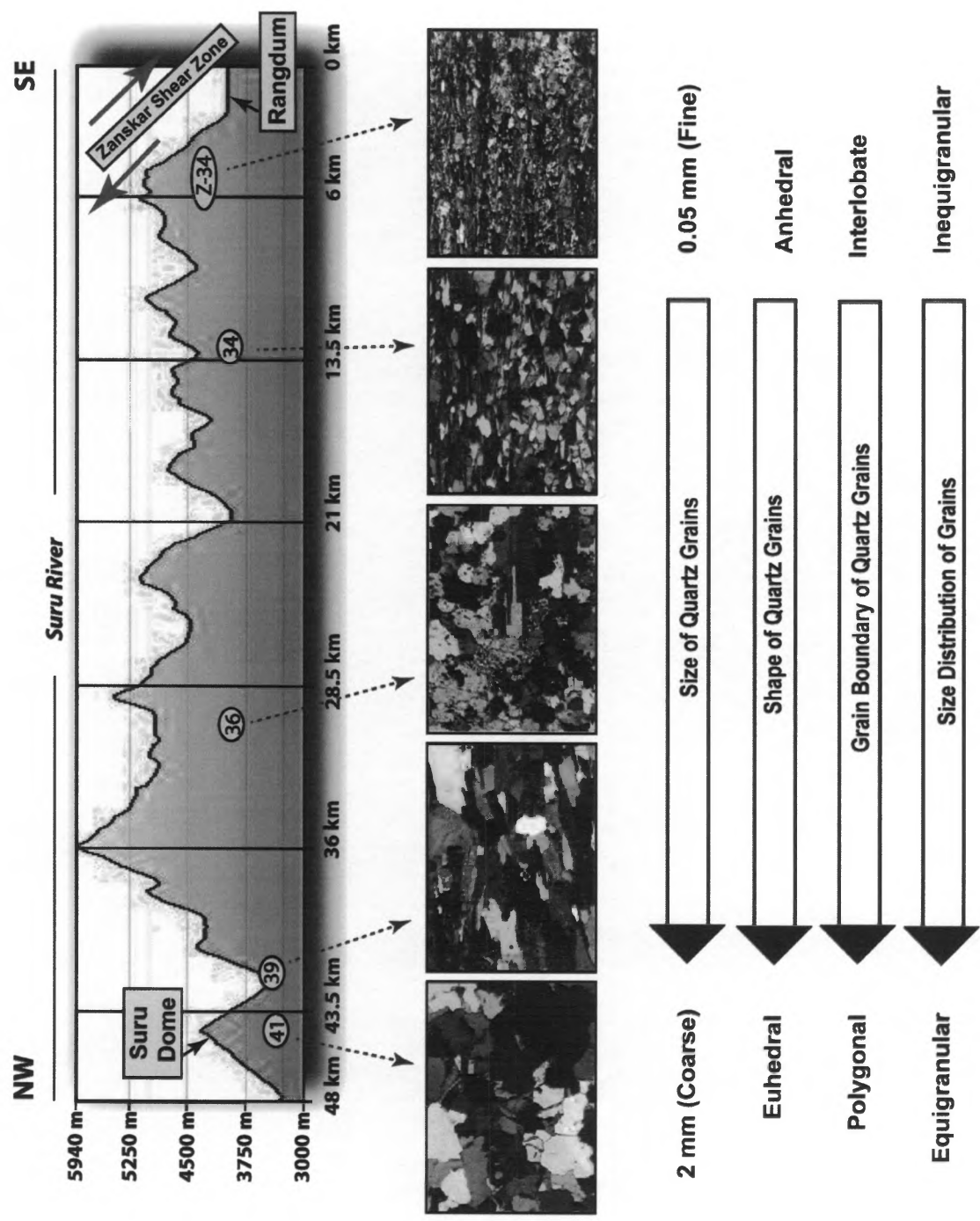


**Figure 8.** Selected sample locations with elevation profile of the Suru Valley and photomicrographs showing textural changes with the distance from the ZSZ. Scale bar in each photomicrograph is 0.4 mm. Note that there is a clear grain-size reduction from Rangdum in the immediate footwall of the ZSZ to the Suru Dome. Cracking or dislocation creep generates more grain-boundary area closer to the ZSZ. Microtextural analyses are summarized (nomenclature after Passchier and Trouw, 2005) based on the distance from the ZSZ.

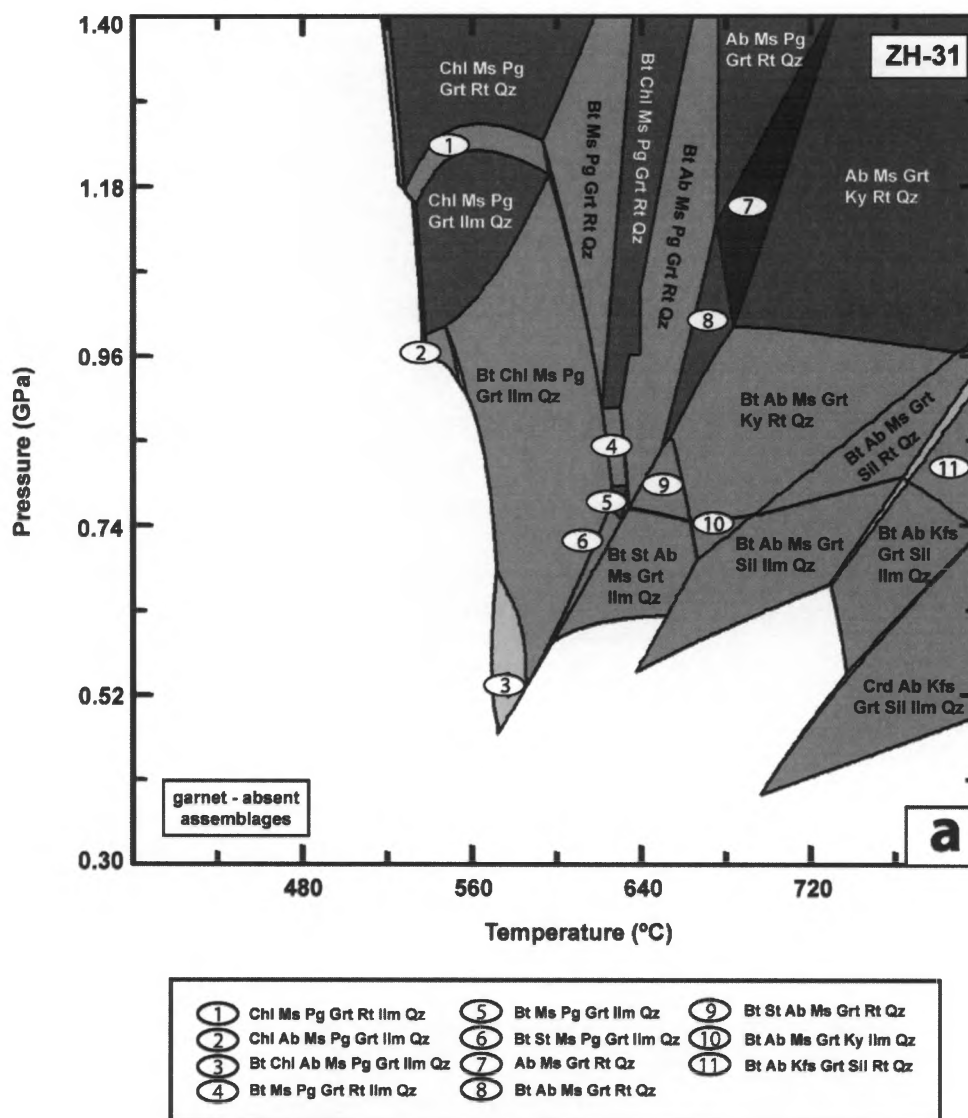


**Figure 9.** (a) Pseudosection for sample ZH-31 showing garnet-bearing assemblages. Garnet-absent fields are ignored for clarity in the figure. Mineral abbreviations from Whitney and Evans (2010), see also Table 2.

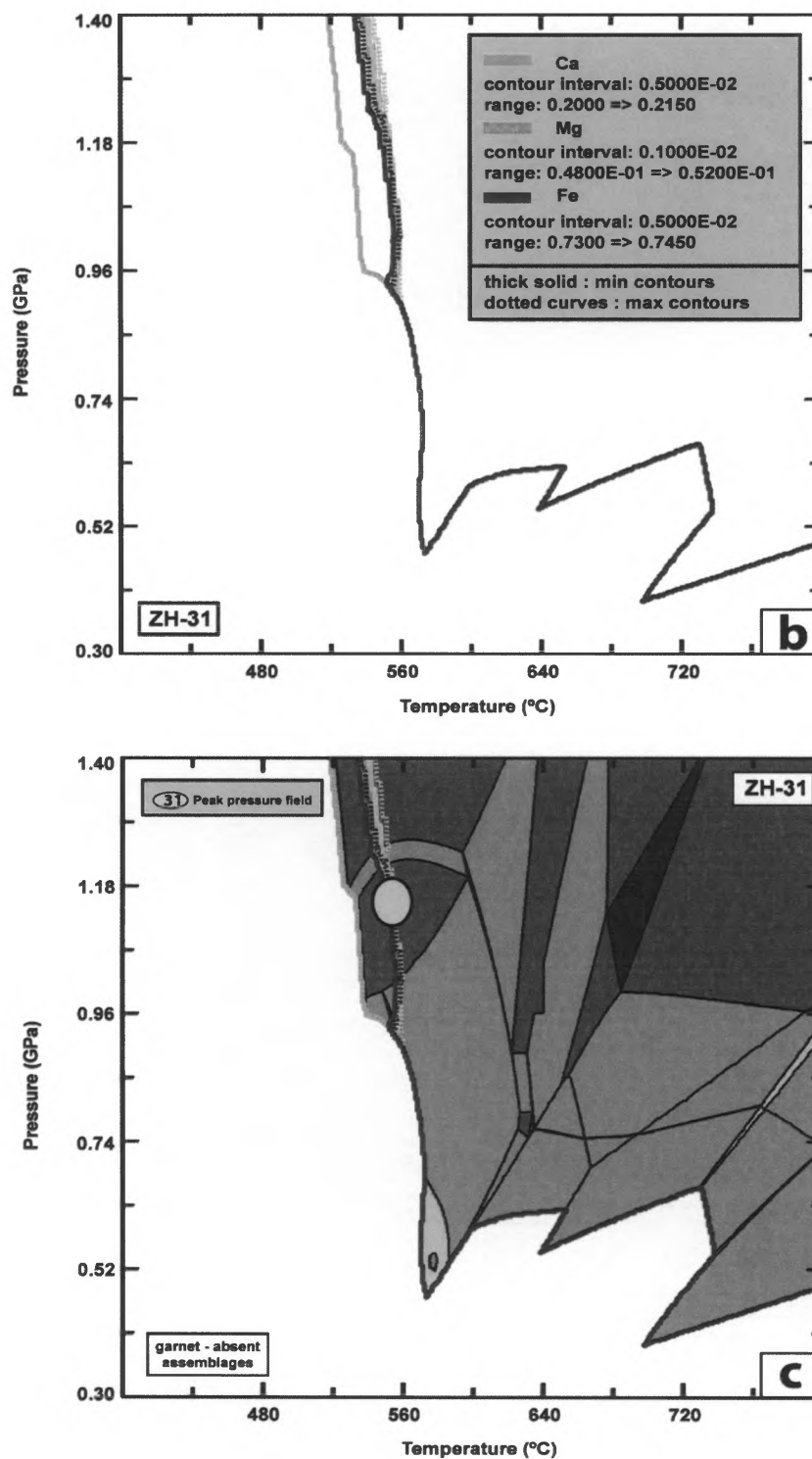


**Figure 9.** (b) Compositional isopleths for Ca, Mg, and Fe components. (c) Isopleths combined with the pseudosection indicates a peak pressure of ~1.18 GPa which is determined by isopleth intersections with the corresponding mineral assemblage.

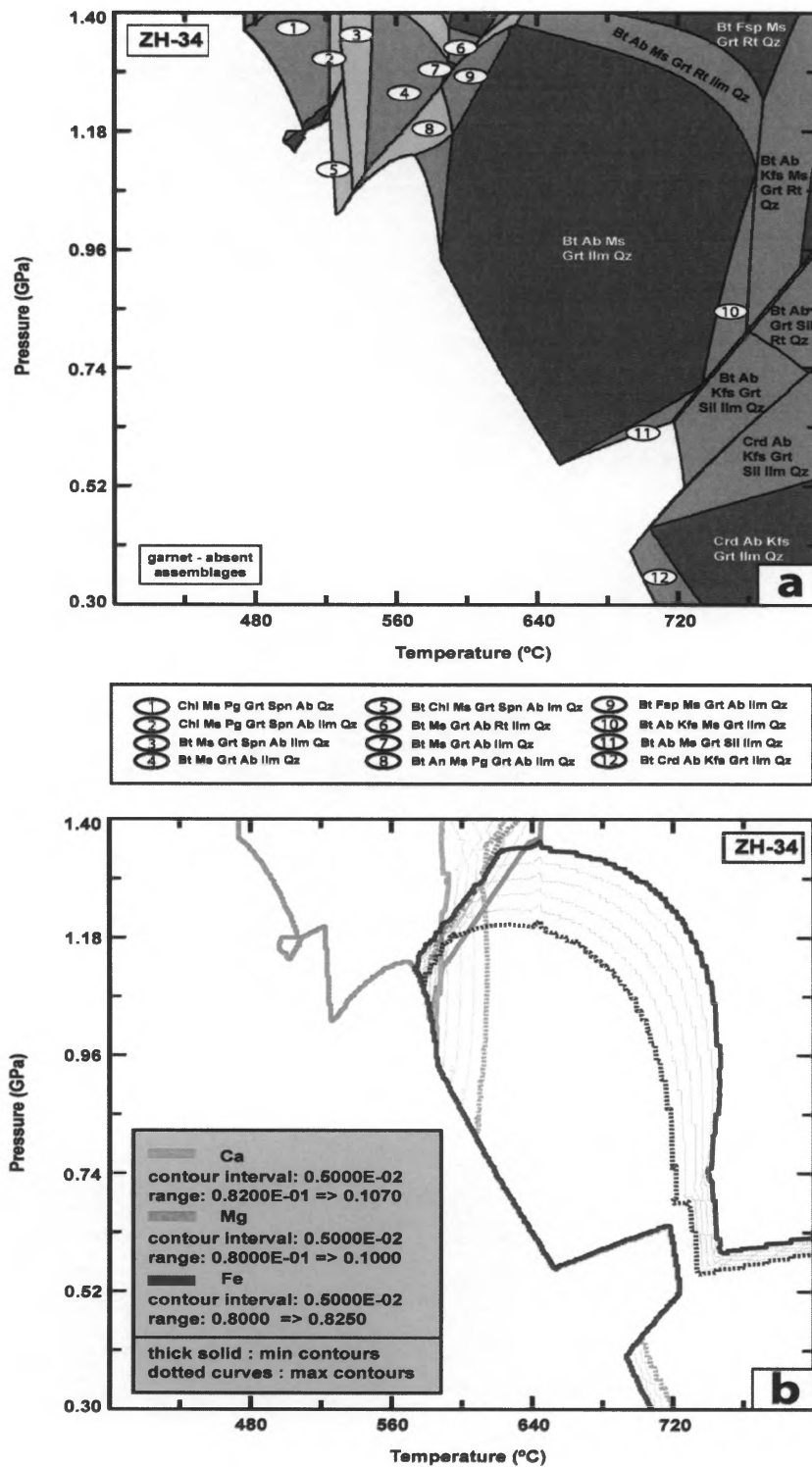


**Figure 10.** (a) Pseudosection for sample ZH-34 showing garnet-bearing assemblages. (b) Compositional isopleths for Ca, Mg, and Fe components. Garnet-absent fields are ignored for clarity in the figure. Mineral abbreviations from Whitney and Evans (2010), see also Table 2.

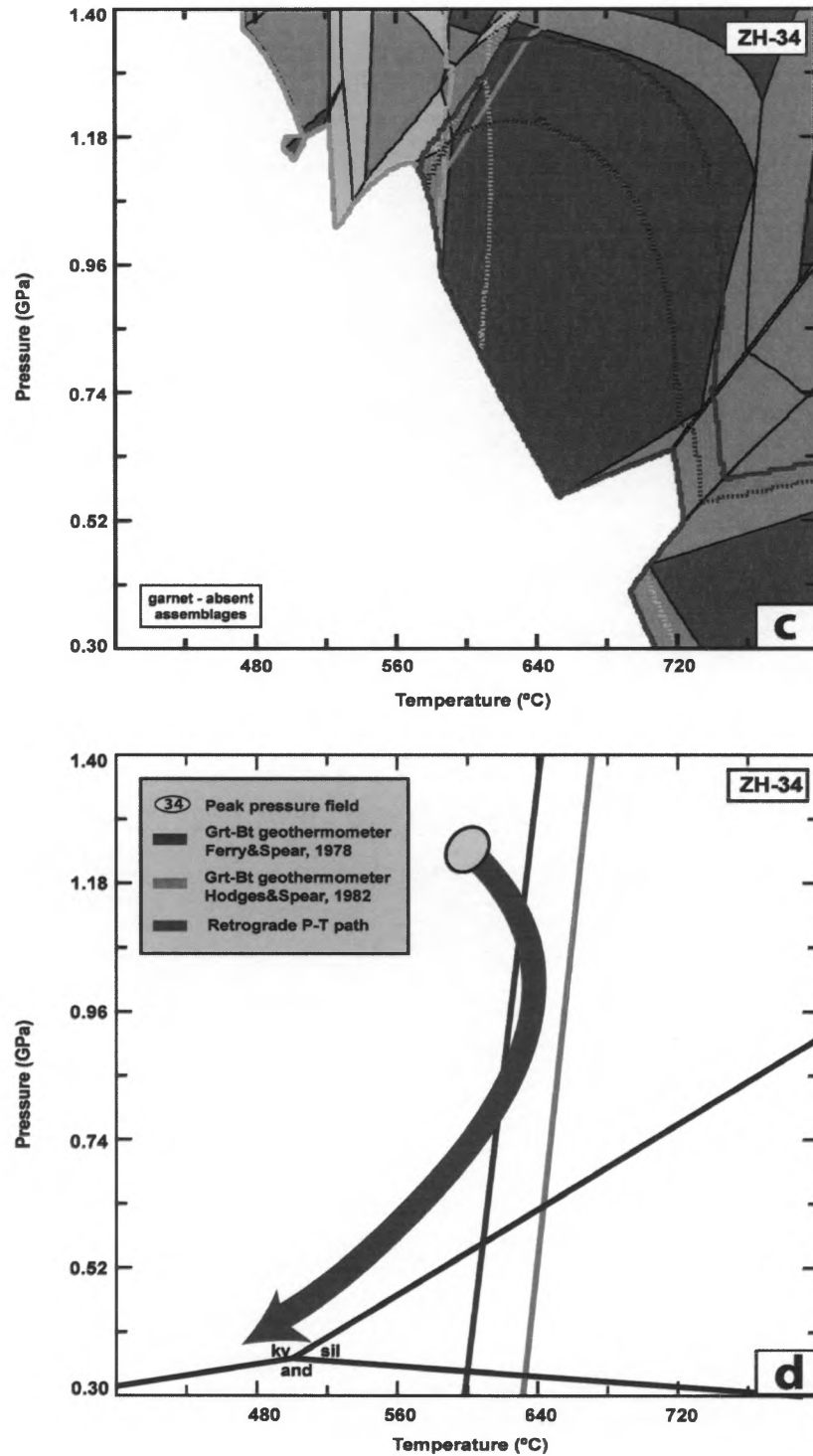


**Figure 10.** (c) Isopleths combined with the pseudosection. Minor fields are unlabelled for clarity. (d) Peak pressure conditions of ~1.23 GPa for ZH-34 and retrograde P-T path, constructed from isopleth intersections with the corresponding mineral assemblage, and peak temperature conditions of <640 °C constrained by Grt-Bt thermometry.

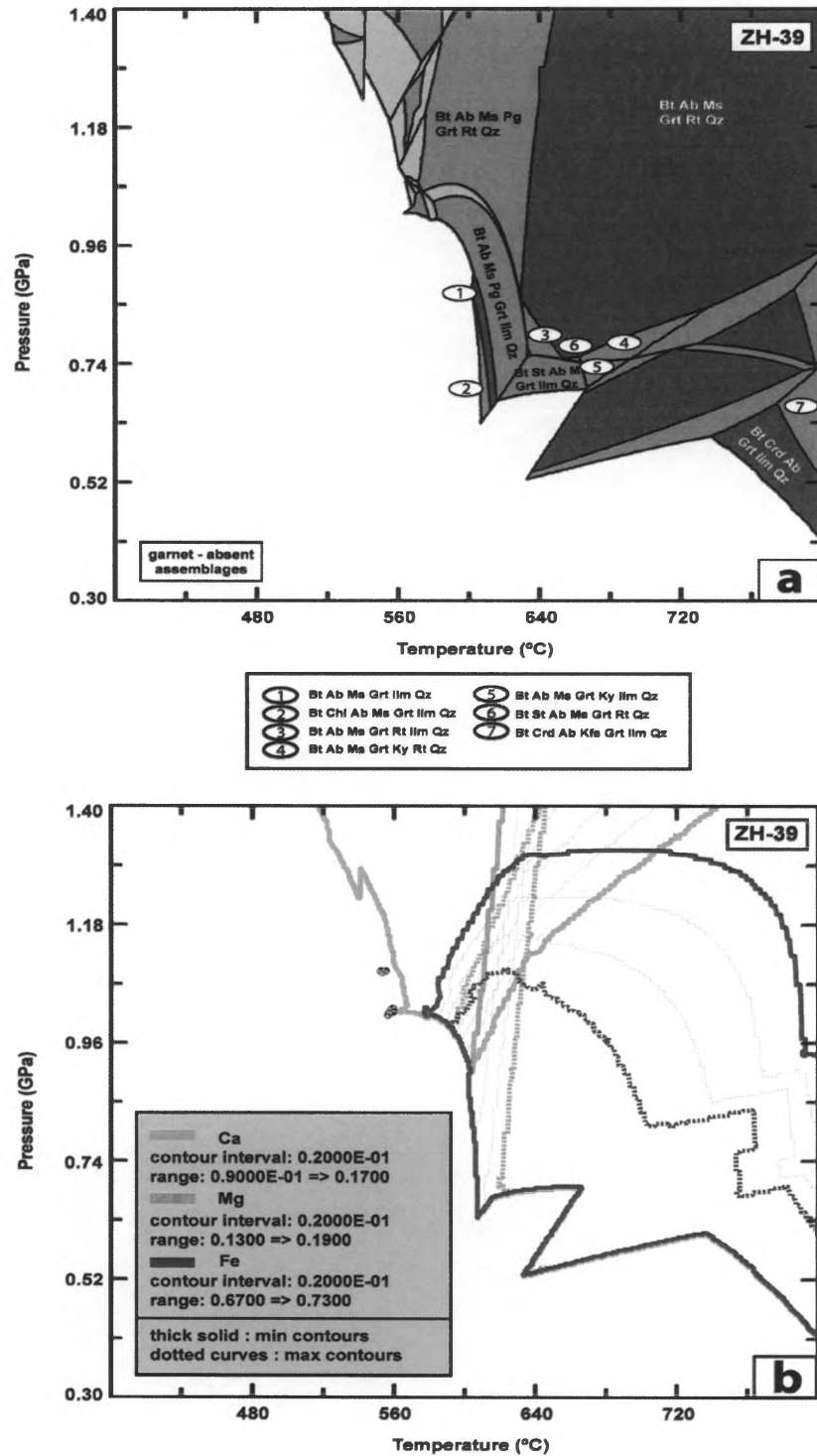


**Figure 11.** (a) Pseudosection for sample ZH-39 showing garnet-bearing assemblages. (b) Compositional isopleths for Ca, Mg, and Fe components. Garnet-absent fields are ignored for clarity in the figure. Mineral abbreviations from Whitney and Evans (2010), see also Table 2.

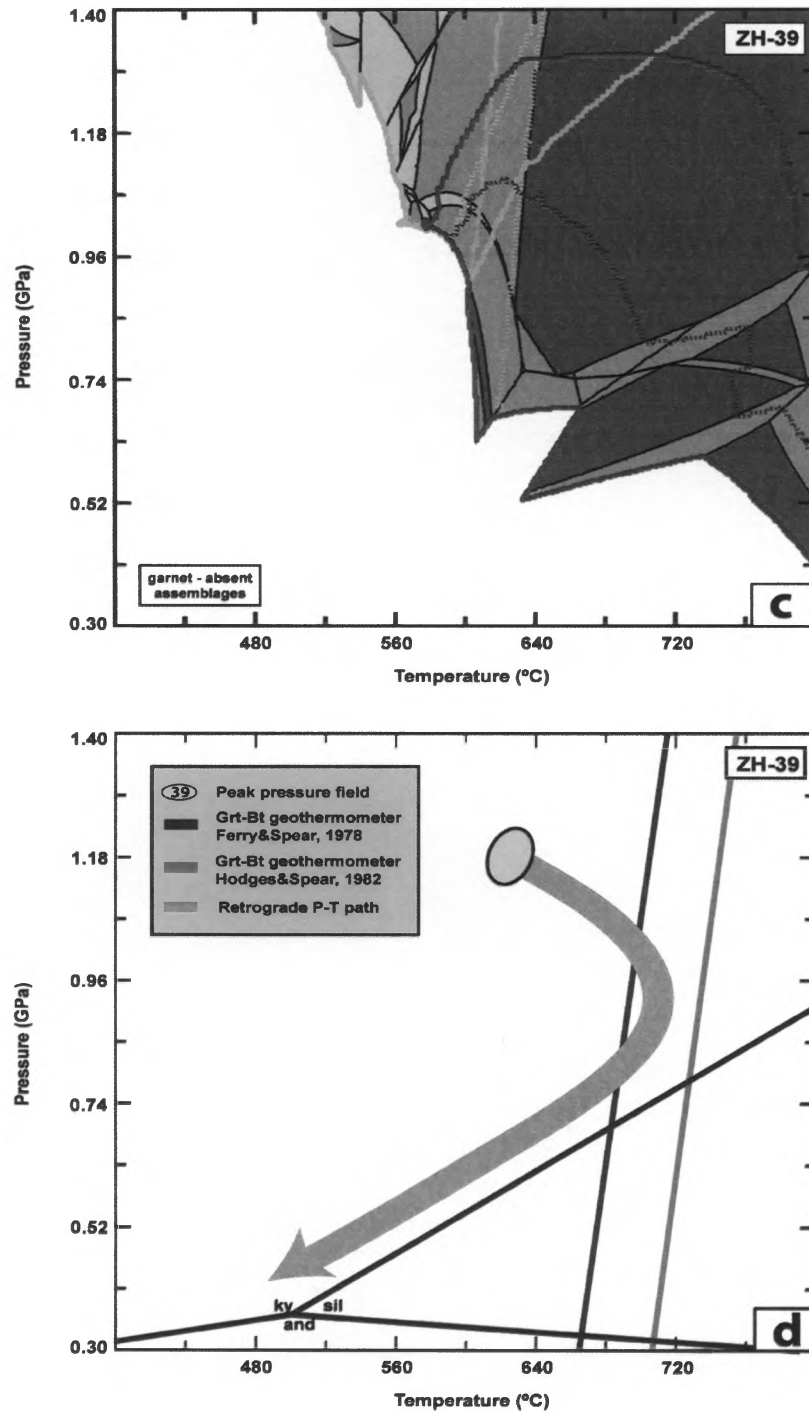


**Figure 11.** (c) Isopleths combined with the pseudosection. High temperatures fields containing sillimanite are unlabelled for clarity due to lack of sillimanite in this sample. (d) Peak pressure conditions of ~1.10 GPa for ZH-39 and retrograde P-T path, constructed from isopleth intersections with the corresponding mineral assemblage, and peak temperature conditions of <720 °C constrained by Grt-Bt thermometry.

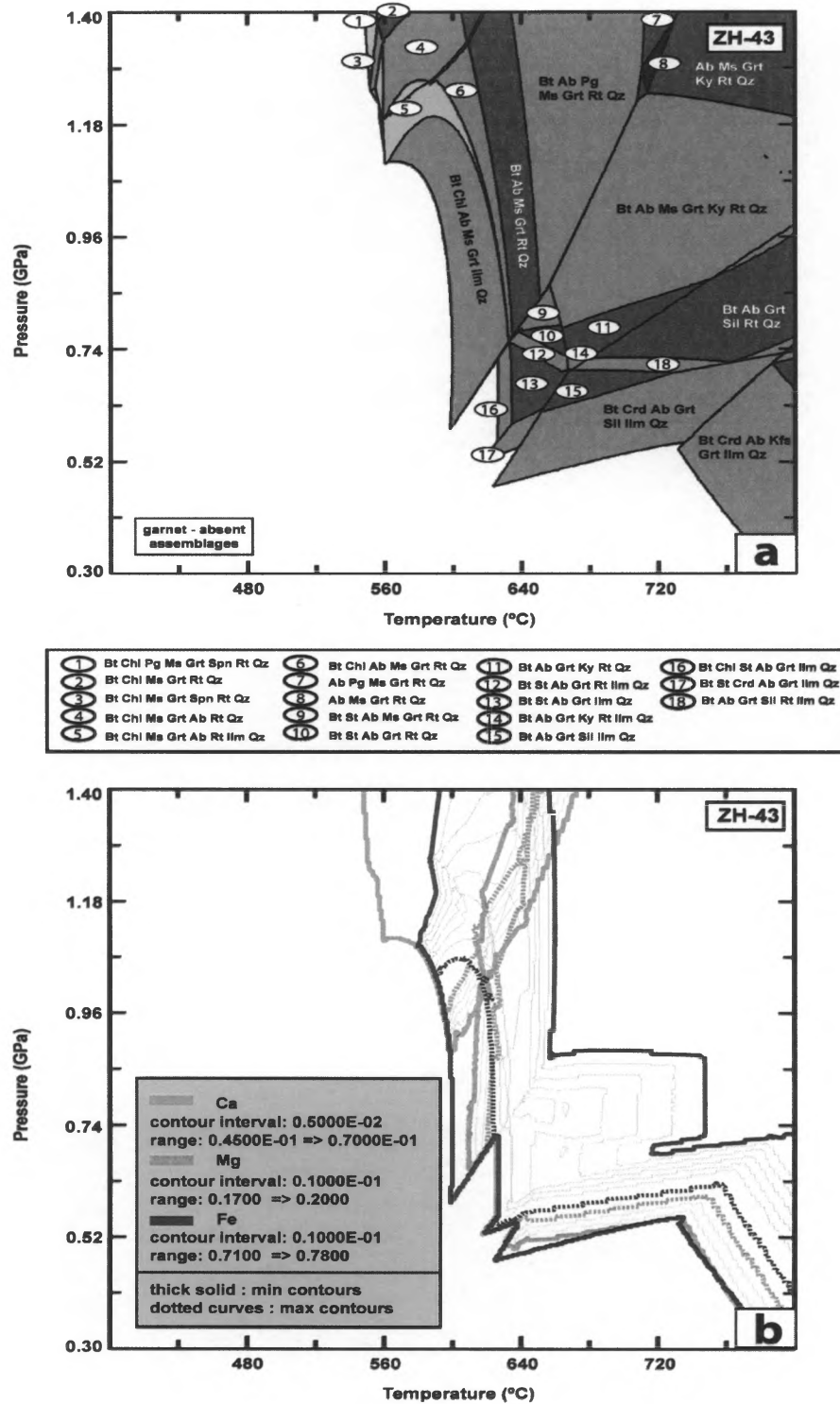


**Figure 12.** (a) Pseudosection for sample ZH-43 showing garnet-bearing assemblages. (b) Compositional isopleths for Ca, Mg, and Fe components. Garnet-absent fields are ignored for clarity in the figure. Mineral abbreviations from Whitney and Evans (2010), see also Table 2.

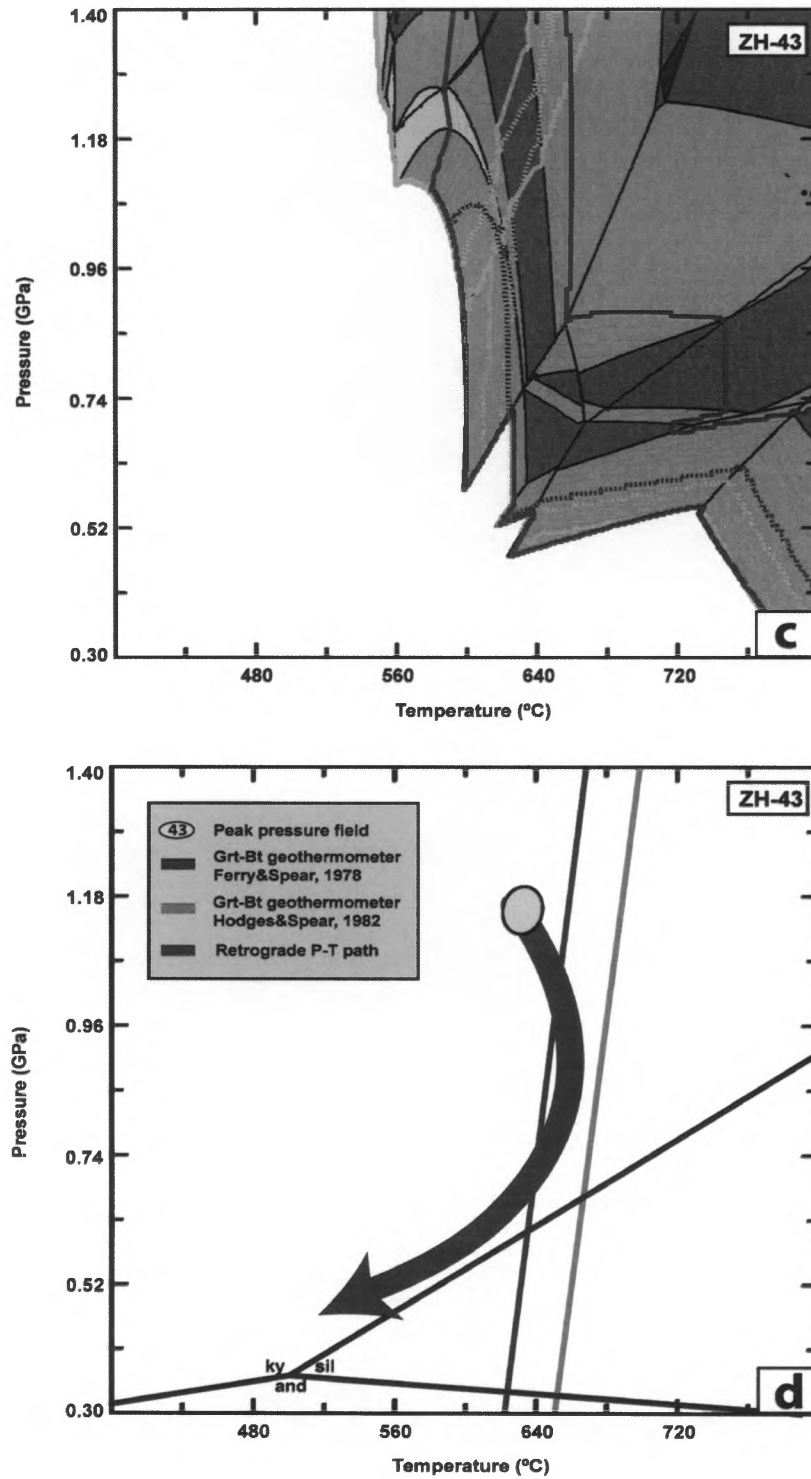


**Figure 12.** (c) Isopleths combined with the pseudosection. (d) Peak pressure conditions of ~1.10 GPa for ZH-43 and retrograde P-T path, constructed from isopleth intersections with the corresponding mineral assemblage, and peak temperature conditions of <680 °C constrained by Grt-Bt thermometry.

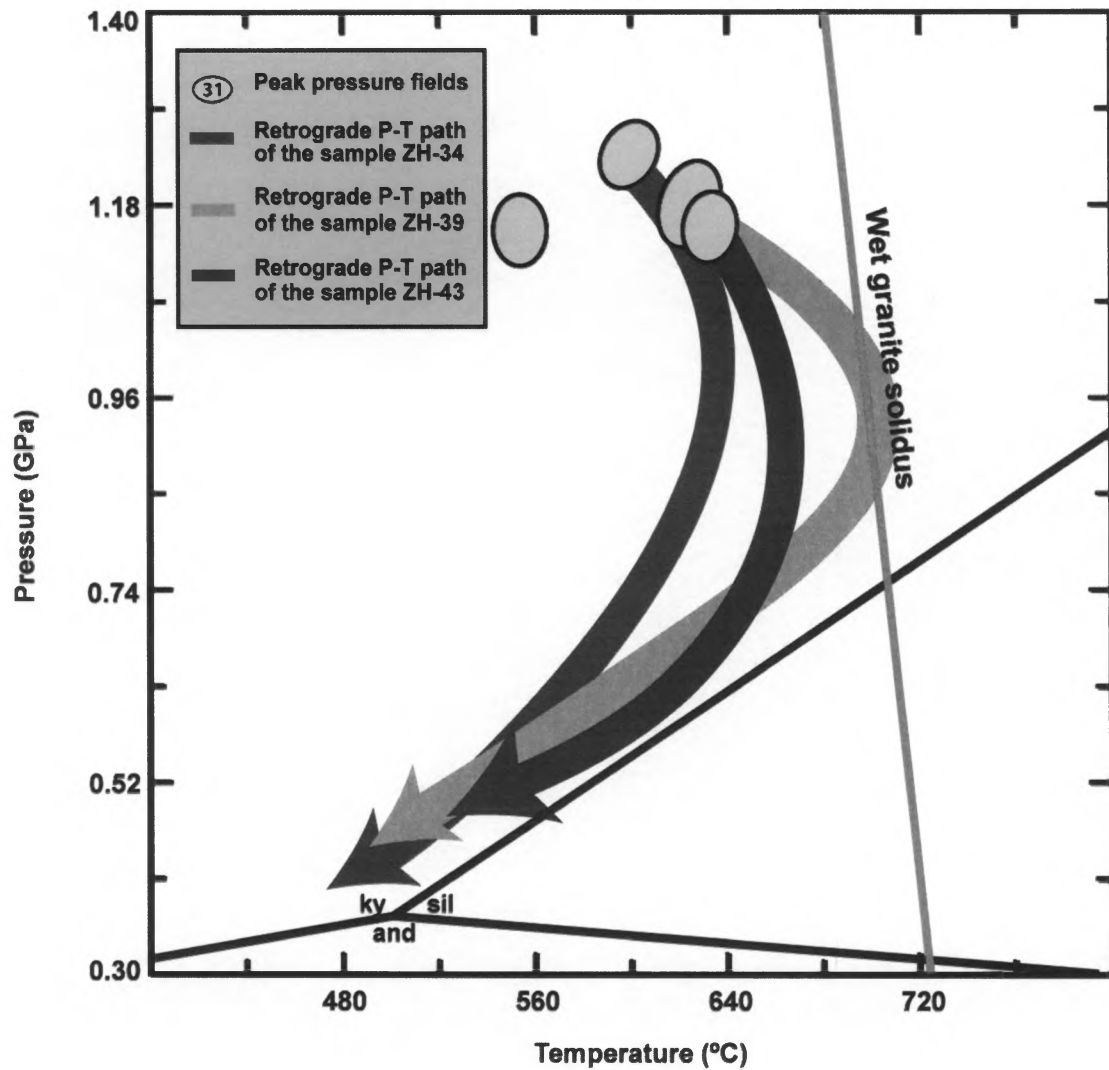


**Figure 13.** Combination of P-T paths interpreted from pseudosection modeling for samples ZH-31, ZH-34, ZH-39 and ZH-43. The peak pressures range from 1.10 to 1.23 GPa, and temperatures range from 620 °C to 700 °C.

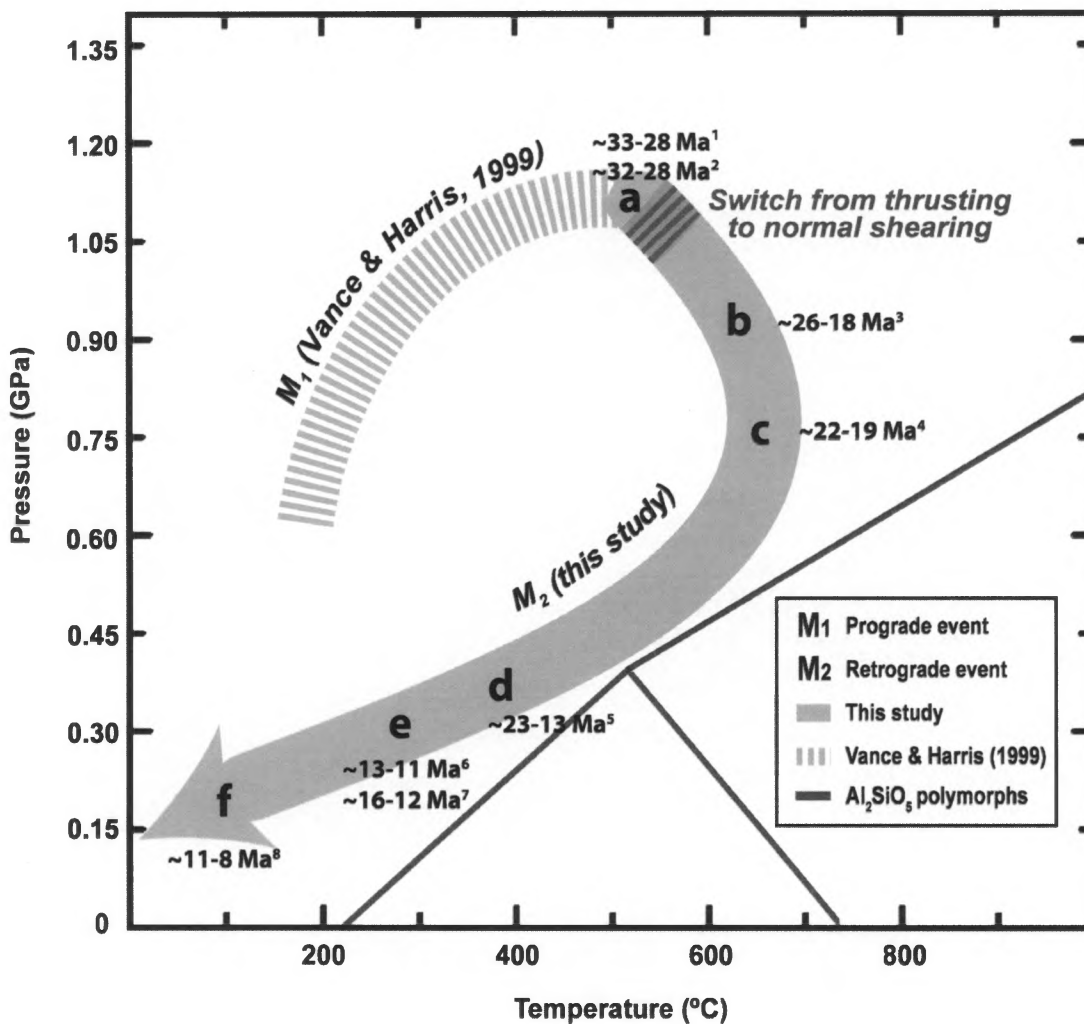


**Figure 14.** Metamorphic modeling showing M<sub>1</sub> and M<sub>2</sub> events. Retrograde path is drawn as a result of this study by combining all P-T paths. Prograde part of the path is from Vance and Harris (1999) due to lack of strong zoning in garnet in this study. Geo/thermochronological data were included on the P-T path: <sup>1</sup> Sm-Nd Garnet from Vance and Harris (1999), <sup>2</sup> U-Pb Monazite from Walker et al (1999), <sup>3</sup> U-Pb Monazite from Horton and Leech (2013), <sup>4</sup> U-Pb Zircon from this study, <sup>5</sup> K-Ar Muscovite from Searle et al (1992), <sup>6</sup> Rb-Sr Biotite from Honegger et al (1982), <sup>7</sup> Rb-Sr Biotite from Inger (1998), <sup>8</sup> AFT Apatite from Sorkhabi et al (1997).

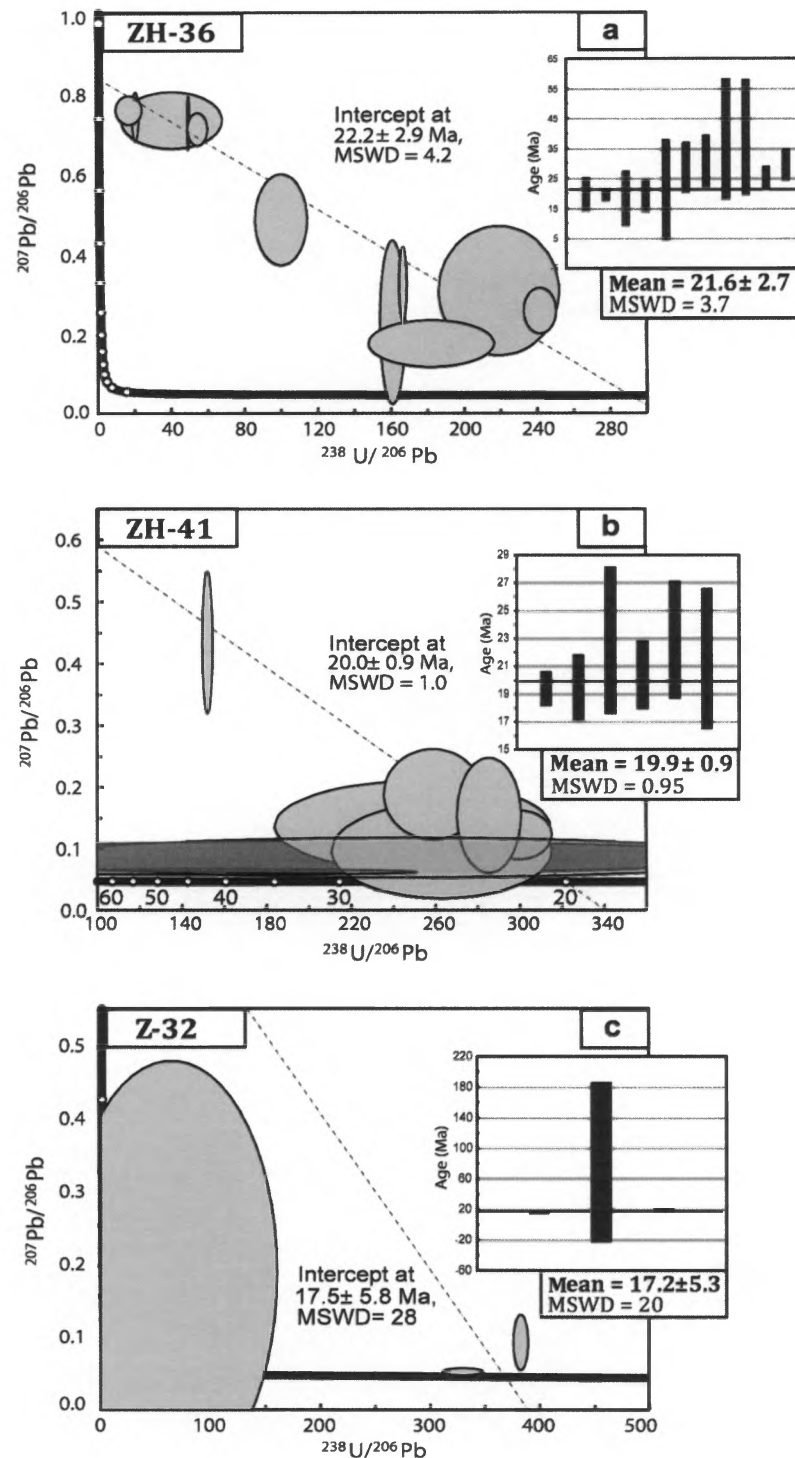


**Figure 15.** Results of zircon U-Pb geochronology for schist samples ZH-36 (a), ZH-41 (b), and Z-32 (c). Tera-Wasserburg concordia plot for all analyses. Data-point error ellipses are  $2\sigma$ . Dark gray ellipses indicate analyses with large errors and are not included in the weighted mean age estimate. Weighted mean average histogram plots of  $^{206}\text{Pb}/^{238}\text{U}$  ages for zircon have  $2\sigma$  error bars.

## TABLES

Table 1. Representative samples from Suru Valley.

Sample No	Location	Latitude/ Longitude	Mineral Assemblage
Z-34	Rangdum	N34°03'25'' E76°19'57''	Qz+Chl+Cld+Bt+Ms+Ep+Rt
ZH-31	Rangdum-Shafat	N34°03'20'' E76°18'38''	Qz+Ms+Chl+Gr+Grt+Ilm+Rt+Tur
ZH-33	Rangdum-Shafat	N34°03'21'' E76°17'33''	Qz+Grt+Bt+Ms
ZH-34	Rangdum-Shafat	N34°02'43'' E76°15'23''	Qz+Bt+Ms+Grt+Ab+Ap+Ilm+Tur
ZH-35	Rangdum-Shafat	N34°03'49'' E76°11'16''	Qz+Bt+Kfs+Grt+Pl+Tur+Rt
ZH-36	Shafat-Parkachik	N 34°04'56'' E76°05'23''	Qz+Bt+St+Pl+Grt+Ms+Chl+Crd+Ttn+Tur+Zrn
ZH-39	Parkachik-Tangol	N34°05'26'' E76°00'22''	Qz+Bt+Ms+St+Grt+Ab+Prg+Chl+Tpz+Zo+Ky+Di+And+Ilm+Tur+Rt
ZH-41	Parkachik-Tangol	N34°03'13'' E75°57'14''	Qz+Bt+Ms+Sil+Ilm+St+Chl+Ky+And+Crd+Grt+Kfs+Tur
ZH-43	Panikhar-Sankoo	N34°08'46'' E75°57'6''	Qz+Bt+Chl+St+Ky+And+Grt+Kfs+Rt+Zrn
ZH-45	Panikhar-Sankoo	N34°13'6'' E75°57'6''	Qz+Bt+Ms+Kfs+Chl+Grt+Pl+Cal+Rt+Tur+Zo

Note: See Table 2 for mineral abbreviations (after Whitney and Evans, 2010) and Figure 2 for the locations.

**Table 2.** Mineral abbreviations used in this study (from Whitney and Evans, 2010).

<b>Symbol</b>	<b>Mineral</b>
Ab	Albite
And	Andalusite
Ap	Apatite
Bt	Biotite
Cal	Calcite
Chl	Chlorite
Crd	Cordierite
Di	Diopside
Ep	Epidote
Gr	Graphite
Grt	Garnet
Ilm	Ilmenite
Kfs	K-feldspar
Ky	Kyanite
Pg	Paragonite
Pl	Plagioclase
Qz	Quartz
Rt	Rutile
Ms	Muscovite
Sil	Sillimanite
St	Staurolite
Ttn	Titanite
Tur	Tourmaline
Zo	Zoisite
Zrn	Zircon

**Table 3.** Whole-rock geochemical data for ten samples from the Suru Valley.

	ZH-31	ZH-32	ZH-33	ZH-34	ZH-35	ZH-36	ZH-39	ZH-41	ZH-43	ZH-45
<b>Unnormalized Major Elements (Weight %)</b>										
<b>SiO<sub>2</sub></b>	60.74	23.07	69.64	68.72	75.96	75.14	60.54	65.35	73.83	70.58
<b>TiO<sub>2</sub></b>	0.815	0.356	0.756	0.620	0.521	0.403	0.827	0.917	0.746	0.345
<b>Al<sub>2</sub>O<sub>3</sub></b>	20.20	7.67	13.39	16.18	10.26	7.38	18.79	15.49	13.34	7.81
<b>FeO*</b>	6.31	2.74	6.16	4.34	3.93	3.16	6.16	6.73	4.74	3.89
<b>MnO</b>	0.090	0.044	0.116	0.073	0.043	0.074	0.103	0.089	0.067	0.114
<b>MgO</b>	1.96	1.72	2.65	1.16	3.59	3.33	3.10	3.17	2.20	2.42
<b>CaO</b>	0.74	33.44	0.79	0.63	0.30	6.68	1.98	0.83	0.52	5.56
<b>Na<sub>2</sub>O</b>	1.37	0.91	1.97	2.71	2.08	1.22	4.13	1.32	1.97	0.73
<b>K<sub>2</sub>O</b>	3.15	0.83	3.72	3.64	2.16	1.33	2.82	3.88	1.41	1.41
<b>P<sub>2</sub>O<sub>5</sub></b>	0.118	0.089	0.119	0.053	0.077	0.129	0.125	0.186	0.190	0.104
<b>Sum</b>	95.49	70.87	99.32	98.12	98.93	98.86	98.58	97.97	99.01	92.96
<b>LOI (%)</b>	3.77	27.93	1.07	1.93	1.05	1.37	1.35	1.80	0.67	6.85
<b>Unnormalized Trace Elements (ppm)</b>										
<b>Ni</b>	18	18	44	19	18	18	47	32	29	26
<b>Cr</b>	87	48	88	49	27	36	101	94	73	52
<b>Sc</b>	17	7	14	14	7	7	17	16	13	11
<b>V</b>	116	53	102	67	46	53	109	105	70	57
<b>Ba</b>	380	104	705	709	144	340	384	951	356	547
<b>Rb</b>	137	43	164	151	86	45	176	169	63	44
<b>Sr</b>	352	1981	69	125	31	163	108	98	52	154
<b>Zr</b>	171	110	237	190	247	285	199	220	425	98
<b>Y</b>	33	18	28	36	19	23	36	34	47	22
<b>Nb</b>	15.2	9.2	12.3	13.5	8.2	7.7	17.8	17.9	15.8	8.4
<b>Ga</b>	24	9	18	21	10	10	23	22	14	10
<b>Cu</b>	11	8	12	9	2	6	8	30	13	57
<b>Zn</b>	114	28	97	96	52	51	66	86	36	30
<b>Pb</b>	25	13	15	20	8	17	31	21	8	14
<b>La</b>	49	22	33	42	19	24	52	42	58	27
<b>Ce</b>	103	42	67	83	38	49	99	83	120	51
<b>Th</b>	19	10	16	17	10	12	25	18	27	9
<b>Nd</b>	41	17	31	37	17	21	42	33	50	23
<b>U</b>	3	3	2	3	2	3	6	3	5	3
<b>Cs</b>	4	0	5	26	7	0	7	4	3	1

Note: LOI, Loss on ignition.

Table 4. Representative mineral compositions for Zanskar samples.

Sample	ZH-31					ZH-34							
	Grt core	Grt rim	Chl	Chl	Ilm	Grt core	Grt rim	Bt	Grt core	Grt rim	Bt	Ms	Ms
SiO <sub>2</sub>	36.79	37.00	22.05	22.09	0.00	36.96	36.69	33.63	36.82	36.35	34.59	45.11	44.77
TiO <sub>2</sub>	0.12	0.09	0.07	0.06	53.59	0.05	0.06	3.09	0.26	0.05	1.69	0.92	0.72
Al <sub>2</sub> O <sub>3</sub>	21.11	21.18	22.45	22.56	0.00	21.10	20.90	18.13	21.18	21.07	18.55	34.50	35.61
Cr <sub>2</sub> O <sub>3</sub>	0.02	0.03	0.02	0.01	0.02	0.01	0.00	0.05	0.04	0.04	0.00	0.00	0.02
FeO	28.61	31.36	26.76	27.18	45.70	32.77	32.82	21.81	32.67	33.20	21.23	2.10	1.84
MnO	5.37	2.67	0.07	0.00	0.83	4.05	4.23	0.17	3.95	4.65	0.22	0.04	0.05
MgO	1.01	1.25	12.66	12.23	0.09	2.05	1.99	6.21	2.11	1.89	7.08	1.14	0.92
CaO	7.00	7.23	0.00	0.00	0.00	3.14	2.94	0.02	2.80	2.57	0.00	0.00	0.01
Na <sub>2</sub> O	0.01	0.02	0.00	0.01	0.02	0.01	0.00	0.11	0.03	0.01	0.11	0.58	0.58
K <sub>2</sub> O	0.00	0.00	0.00	0.00	0.00	0.00	0.00	9.35	0.00	0.00	9.07	10.52	10.42
SUM	100.04	100.83	84.08	84.14	100.25	100.14	99.63	92.57	99.86	99.83	92.54	94.91	94.94
O	12	12	14	14	3	12	12	11	12	12	11	11	11
Si	2.97	2.97	2.47	2.48	0.00	2.99	2.99	2.69	2.98	2.96	2.74	3.04	3.01
Ti	0.01	0.01	0.01	0.01	1.01	0.00	0.00	0.19	0.02	0.00	0.10	0.05	0.04
Al	2.01	2.00	2.96	2.98	0.00	2.01	2.01	1.71	2.02	2.02	1.73	2.74	2.82
Cr	0.00	0.00	0.00	0.00	0.00	0.00	0.00	0.00	0.00	0.00	0.00	0.00	0.00
Fe	1.93	2.10	2.51	2.55	0.96	2.22	2.23	1.46	2.21	2.26	1.41	0.12	0.10
Mn	0.37	0.18	0.01	0.00	0.02	0.28	0.29	0.01	0.27	0.32	0.02	0.00	0.00
Mg	0.12	0.15	2.11	2.04	0.00	0.25	0.24	0.74	0.25	0.23	0.84	0.11	0.09
Ca	0.61	0.62	0.00	0.00	0.00	0.27	0.26	0.00	0.24	0.22	0.00	0.00	0.00
Na	0.00	0.00	0.00	0.00	0.00	0.00	0.00	0.02	0.01	0.00	0.02	0.08	0.08
K	0.00	0.00	0.00	0.00	0.00	0.00	0.00	0.95	0.00	0.00	0.92	0.90	0.89
SUM	20.02	20.03	24.07	24.06	4.99	20.02	20.02	18.77	20.00	20.01	18.78	18.04	18.03
X <sub>Mg</sub>	0.06	0.07	0.46	0.45	-	0.10	0.10	0.34	0.10	0.09	0.37	0.49	0.47
X <sub>Ca</sub>	-	-	-	-	-	-	-	-	-	-	-	-	-
Al(IV)	-	-	-	-	-	-	-	1.31	-	-	1.26	0.96	0.99
Al(VI)	-	-	-	-	-	-	-	0.39	-	-	0.47	1.78	1.83
Alm	0.64	0.69	-	-	-	0.74	0.74	-	0.74	0.74	-	-	-
Prp	0.04	0.05	-	-	-	0.08	0.08	-	0.09	0.08	-	-	-
Grs	0.20	0.20	-	-	-	0.09	0.08	-	0.08	0.07	-	-	-
Sps	0.12	0.06	-	-	-	0.09	0.10	-	0.09	0.11	-	-	-

Note:  $X_{Mg} = Mg / (Mg + Fe^{2+})$ ;  $X_{Ca} = Ca / (Ca + Na + K)$ ;  $Al^{(IV)} = (4 - Si)$ ;  $Al^{(VI)} = Al^{total} - Al^{(IV)}$ ;  $Alm = Fe^{2+} / (Ca + Mg + Fe^{2+} + Mn)$ ;  $Prp = Mg / (Ca + Mg + Fe^{2+} + Mn)$ ;  $Grs = Ca / (Ca + Mg + Fe^{2+} + Mn)$ ;  $Sps = Mn / (Ca + Mg + Fe^{2+} + Mn)$ .

Table 4. Representative mineral compositions for Zanskar samples (continued).

Sample	ZH-39							ZH-43							
	Mineral	Grt core	Grt rim	Bt	Grt core	Grt rim	Bt	Als	Grt core	Grt rim	Bt core	Bt rim	Grt core	Grt rim	Bt core
SiO <sub>2</sub>	36.31	36.59	34.17	39.65	37.19	34.89	35.47	37.94	37.71	37.03	35.82	37.91	37.24	35.64	35.67
TiO <sub>2</sub>	0.02	0.03	2.11	0.00	0.01	2.14	0.00	0.03	0.02	1.99	1.48	0.02	0.01	1.75	1.61
Al <sub>2</sub> O <sub>3</sub>	21.03	21.26	19.21	22.51	21.22	18.99	63.58	21.51	21.72	18.32	20.57	20.96	21.41	19.21	20.22
Cr <sub>2</sub> O <sub>3</sub>	0.01	0.03	0.03	0.00	0.01	0.02	0.06	0.03	0.02	0.04	0.02	0.02	0.02	0.02	0.02
FeO	32.95	31.89	16.35	35.02	32.14	16.38	0.13	31.85	33.17	15.57	15.62	32.99	34.21	16.76	15.98
MnO	2.25	0.96	0.09	2.35	0.73	0.12	0.00	1.53	1.28	0.04	0.09	0.95	1.42	0.05	0.07
MgO	3.72	4.11	10.72	4.25	4.13	10.96	0.00	4.75	4.58	11.16	10.49	5.53	4.22	11.55	10.20
CaO	1.96	3.41	0.00	2.04	3.64	0.00	0.02	2.73	2.59	0.12	0.00	1.47	1.54	0.02	0.02
Na <sub>2</sub> O	0.01	0.02	0.20	0.01	0.00	0.32	0.01	0.02	0.00	0.26	0.26	0.00	0.00	0.17	0.22
K <sub>2</sub> O	0.00	0.00	9.57	0.00	0.00	9.39	0.00	0.00	0.00	9.09	9.29	0.00	0.00	9.32	9.30
SUM	98.26	98.30	92.45	105.83	99.07	93.21	99.27	100.39	101.09	93.62	93.64	99.85	100.07	94.49	93.31
O	12	12	11	12	12	11	5	12	12	11	11	12	12	11	11
Si	2.97	2.97	2.66	3.00	2.99	2.68	0.966	3.00	2.97	2.80	2.71	3.01	2.98	2.70	2.72
Ti	0.00	0.00	0.12	0.00	0.00	0.12	0.00	0.00	0.00	0.11	0.09	0.00	0.00	0.10	0.09
Al	2.03	2.03	1.76	2.01	2.01	1.72	2.042	2.00	2.02	1.63	1.84	1.96	2.02	1.71	1.82
Cr	0.00	0.00	0.00	0.00	0.00	0.00	0.001	0.00	0.00	0.00	0.00	0.00	0.00	0.00	0.00
Fe	2.25	2.16	1.06	2.21	2.16	1.05	0.003	2.11	2.19	0.99	0.99	2.19	2.29	1.06	1.02
Mn	0.16	0.07	0.01	0.15	0.05	0.01	0.001	0.10	0.09	0.00	0.01	0.06	0.10	0.00	0.01
Mg	0.45	0.50	1.24	0.48	0.49	1.26	0.00	0.56	0.54	1.26	1.19	0.66	0.50	1.30	1.16
Ca	0.17	0.30	0.00	0.17	0.31	0.00	0.001	0.23	0.22	0.01	0.00	0.13	0.13	0.00	0.00
Na	0.00	0.00	0.03	0.00	0.00	0.05	0.00	0.00	0.00	0.04	0.04	0.00	0.00	0.03	0.03
K	0.00	0.00	0.95	0.00	0.00	0.92	0.00	0.00	0.00	0.88	0.90	0.00	0.00	0.90	0.91
SUM	20.03	20.03	18.83	20.02	20.01	18.81	8.014	20.00	20.03	18.72	18.77	20.01	20.02	18.80	18.76
X <sub>Mg</sub>	0.17	0.19	0.54	0.18	0.19	0.54	-	0.21	0.20	0.56	0.54	0.23	0.18	0.55	0.53
X <sub>Ca</sub>	-	-	-	-	-	-	-	-	-	-	-	-	-	-	-
Al (IV)	-	-	1.34	-	-	1.32	-	-	-	1.20	1.29	-	-	1.30	1.28
Al (VI)	-	-	0.42	-	-	0.40	-	-	-	0.44	0.55	-	-	0.41	0.54
Alm	0.74	0.72	-	0.74	0.72	-	-	0.70	0.72	-	-	0.72	0.76	-	-
Prp	0.15	0.16	-	0.16	0.16	-	-	0.19	0.18	-	-	0.22	0.17	-	-
Grs	0.06	0.10	-	0.05	0.10	-	-	0.08	0.07	-	-	0.04	0.04	-	-
Sps	0.05	0.02	-	0.05	0.02	-	-	0.03	0.03	-	-	0.02	0.03	-	-

Note:  $X_{Mg} = Mg / (Mg + Fe^{2+})$ ;  $X_{Ca} = Ca / (Ca + Na + K)$ ;  $Al^{(IV)} = (4 - Si)$ ;  $Al^{(VI)} = Al^{total} - Al^{(IV)}$ ;  $Alm = Fe^{2+} / (Ca + Mg + Fe^{2+} + Mn)$ ;  $Prp = Mg / (Ca + Mg + Fe^{2+} + Mn)$ ;  $Grs = Ca / (Ca + Mg + Fe^{2+} + Mn)$ ;  $Sps = Mn / (Ca + Mg + Fe^{2+} + Mn)$ .

Table 4. Representative mineral compositions for Zanskar samples (continued).

Sample	ZH-45									
	Mineral	Grt core	Grt rim	Bt	Grt core	Grt rim	Bt	Ms	PI	PI
SiO <sub>2</sub>	37.45	37.70	35.93	37.21	37.64	36.01	45.44	62.69	62.00	
TiO <sub>2</sub>	0.09	0.06	1.65	0.09	0.06	1.49	0.45	0.00	0.00	
Al <sub>2</sub> O <sub>3</sub>	21.60	21.73	18.32	21.53	21.72	19.22	34.83	22.79	22.87	
Cr <sub>2</sub> O <sub>3</sub>	0.02	0.04	0.01	0.03	0.00	0.02	0.07	0.00	0.00	
FeO	29.53	29.30	16.58	29.61	29.18	15.67	1.61	0.00	0.00	
MnO	0.91	0.72	0.01	0.90	0.78	0.02	0.00	0.00	0.00	
MgO	2.84	3.37	11.45	2.86	3.35	12.27	1.55	0.00	0.00	
CaO	7.63	7.87	0.03	7.83	8.00	0.00	0.00	4.09	4.14	
Na <sub>2</sub> O	0.01	0.00	0.09	0.02	0.01	0.13	0.64	9.38	9.51	
K <sub>2</sub> O	0.00	0.00	9.80	0.00	0.00	9.03	10.50	0.15	0.14	
SUM	100.09	100.78	93.86	100.08	100.74	93.87	95.08	99.11	98.66	
O	12	12	11	12	12	11	11	8	8	
Si	2.98	2.97	2.74	2.96	2.97	2.72	3.046	2.80	2.79	
Ti	0.01	0.00	0.10	0.01	0.00	0.09	0.023	0.00	0.00	
Al	2.02	2.02	1.65	2.02	2.02	1.71	2.752	1.20	1.21	
Cr	0.00	0.00	0.00	0.00	0.00	0.00	0.004	0.00	0.00	
Fe	1.96	1.93	1.06	1.97	1.92	0.99	0.09	0.00	0.00	
Mn	0.06	0.05	0.00	0.06	0.05	0.00	0.00	0.00	0.00	
Mg	0.34	0.40	1.30	0.34	0.39	1.38	0.154	0.00	0.00	
Ca	0.65	0.66	0.00	0.67	0.68	0.00	0.00	0.20	0.20	
Na	0.00	0.00	0.01	0.00	0.00	0.02	0.083	0.81	0.83	
K	0.00	0.00	0.96	0.00	0.00	0.87	0.898	0.01	0.01	
SUM	20.02	20.03	18.82	20.03	20.04	18.78	18.049	13.01	13.03	
X <sub>Mg</sub>	0.15	0.17	0.55	0.15	0.17	0.58	0.63	-	-	
X <sub>Ca</sub>	-	-	-	-	-	-	-	0.19	0.19	
Al (IV)	-	-	1.26	-	-	1.28	0.95	-	-	
Al (VI)	-	-	0.39	-	-	0.43	1.80	-	-	
Alm	0.65	0.64	-	0.65	0.63	-	-	-	-	
Prp	0.11	0.13	-	0.11	0.13	-	-	-	-	
Grs	0.22	0.22	-	0.22	0.22	-	-	-	-	
Sps	0.02	0.02	-	0.02	0.02	-	-	-	-	

Note:  $X_{Mg} = Mg / (Mg + Fe^{2+})$ ;  $X_{Ca} = Ca / (Ca + Na + K)$ ;  $Al^{(IV)} = (4 - Si)$ ;  $Al^{(VI)} = Al^{total} - Al^{(IV)}$ ;  $Alm = Fe^{2+} / (Ca + Mg + Fe^{2+} + Mn)$ ;  $Prp = Mg / (Ca + Mg + Fe^{2+} + Mn)$ ;  $Grs = Ca / (Ca + Mg + Fe^{2+} + Mn)$ ;  $Sps = Mn / (Ca + Mg + Fe^{2+} + Mn)$ .

**Table 5.** Summary U-Pb SHRIMP analyses of zircon.

Spot Number	U (ppm)	Th (ppm)	$^{232}\text{Th}/^{238}\text{U}$	Common $^{206}\text{Pb}$ (%)	Ratios				$^{207}\text{Pb}$ -Corrected Age (Ma)	
					$^{238}\text{U}/^{206}\text{Pb}$	% error	$^{207}\text{Pb}/^{206}\text{Pb}$	% error	$^{206}\text{Pb}/^{238}\text{U}$	1 $\sigma$ error
<b>Sample ZH-36 (Schist)</b>										
1.1	41	0	0.004	86.64	40	27.8	0.7314	4.0	21.3	8.3
5.1	78	0	0.005	26.66	241	1.5	0.2572	9.0	19.6	0.8
6.1	58	0	0.008	22.98	161	1.7	0.2284	36.3	30.8	4.2
7.1	56	1	0.013	35.11	166	23.5	0.3242	31.4	25.1	1.8
8.1a	107	0	0.004	83.77	55	4.1	0.7086	2.3	19.1	2.6
8.1b	40	0	0.004	16.28	182	7.7	0.1754	13.6	29.6	2.5
9.1	64	0	0.007	89.66	17	17.0	0.7563	1.9	38.9	9.5
12.1	70	0	0.007	55.28	100	5.8	0.4838	9.5	28.7	4.1
18.1	74	0	0.005	32.88	219	6.1	0.3063	21.4	19.7	2.7
19.1	29	0	0.006	87.62	21	3.6	0.7402	3.4	38.3	9.9
24.1	48	0	0.006	85.84	50	0.5	0.7249	3.8	18.4	4.5
<b>Sample ZH-41 (Schist)</b>										
3.1	1066	6	0.006	9.73	299	0.5	0.1233	2.1	19.4	0.6
5.1	877	6	0.008	49.13	152	0.6	152.0862	10.8	21.5	2.5
8.1	1392	10	0.007	6.43	263	8.1	0.0973	32.4	22.9	2.1
10.1	994	8	0.008	11.58	249	10.7	0.1380	21.3	22.9	2.6
18.1	1035	5	0.005	13.81	285	2.2	0.1556	24.4	19.4	1.2
21.1	1377	6	0.005	18.07	259	3.6	0.1893	15.9	20.4	1.2
<b>Sample Z-32 (Schist)</b>										
5.1	1539	2185	1.466	0.72	330	2.3	0.0521	3.8	19.4	0.4
10.1	777	19	0.026	5.83	382	0.7	0.0924	16.6	15.9	0.3
11.1	62	2	0.030	17.69	65	60.9	0.1880	63.2	81.7	51.7

**Table 6.** Tectonometamorphic evolution of the Zaskar GHS (compiled from Dèzes (1999), Walker et al. (1999), Walker et al. (2001), and this study).

TIME	TECTONOMETAMORPHIC EPISODE	DEFORMATION		METAMORPHISM		
Pre-55 Ma	Crustal thickening		The THS and the GHS were not differentiated.		Onset of metamorphism	
~55-50 Ma			N-S directed collision of the Indian and Asian continental plates			
~50-33 Ma		D <sub>1</sub>		Continuing burial	M <sub>1</sub>	A prograde Barrovian-type regional metamorphic event: -Metamorphic gradient increases southwards, from chlorite-biotite zone to kyanite zone. -Peak metamorphic conditions around 550-650 °C and 0.8-1.2 GPa.
~33-25 Ma				A top-to-the-SW thrusting of the ZSZ: -Burial and heating of the Suru valley rocks as underthrusting below the THS along the ZSZ. -Large-scale recumbent folds.		
~25-0 Ma	Exhumation	D <sub>2</sub>	A top-to-the NE normal shearing of the ZSZ: -The most rapid exhumation of the GHS. -Coeval movements on the ZSZ and the MCT. -Reactivation of the ZSZ leading to shear the isograds.	M <sub>2</sub>	Retrograde metamorphic event: -Growth of medium-low pressure minerals (the succession of sillimanite, cordierite, k-feldspar, andalusite). -Leucogranite generation -Partial melting of the highest grade M <sub>2</sub> rocks (migmatites).	
			-The Suru Dome -Large-scale doming of the GHS			
			Continued uplift and erosion with minor amounts of brittle normal faulting along the ZSZ.		A late-stage retrogressive phase, responsible for chloritization of garnet, biotite, and staurolite.	